Università degli Studi di Parma

Dottorato in Scienza e Tecnologia dei Materiali Innovativi
Ciclo XXI, 2006-2008

Ferroelectricity and Polymorphism in organic materials: Infrared and Raman spectroscopy of charge-transfer crystals and organic semiconductors

Dottorando: **Dr. Paolo Ranzieri**

Tutor: **Prof. Alberto Girlando**

Coordinatore: **Prof. Anna Painelli**

Parma - 2009

Contents

Preface

For the past fifty years inorganic silicon and gallium arsenide semiconductors, silicon dioxide insulators, and metals such as aluminum and copper have been the backbone of the semiconductor industry. However, we have recently witnessed the development of an intense research effort in the field of "organic electronics", to improve the semiconducting, conducting, and light emitting properties of organics through novel synthesis and self-assembly techniques. Performance improvements, coupled with the ability to process these materials at low temperatures over large areas on materials such as plastic or paper, provide unique technologies and generate new applications.

The rapidly growing field of organic electronics requires a set of versatile functionalities. Apart from single component organic semiconductors, one has to consider binary- or multi-component system such as donor (D)-acceptor (A) molecular compounds. Away from the individual molecular properties of the constituent D and A in the crystal, the intermolecular interactions extensively provides novel functionalities such as conducting, dielectric, magnetic, and optical properties. The representative examples are the charge-transfer (CT) complexes, in which electron transfer between the D and A molecules plays the critical roles. It is increasingly important for organic electronics to investigate how to control these properties in a desired way in response to various external stimuli, such as electric, magnetic, mechanical, optical, thermal, and/or chemical ones. On the other hand improvement of devices, like transistors, based on single component organics, requires tools for improving sample preparation, coupled with an understanding on the carrier mobility mechanism.

In this thesis we will consider two classes of organic materials: mixed-stack D-A CT crystals and single component semiconductors. The first part of the thesis will be devoted to the neutral-ionic phase transition, an interesting type of phase transition that may occur in mixed-stack CT crystals. Among the reasons of interest, we mention the potentially ferroelectric ground state of the ionic (low-temperature) phase. We shall first consider the temperature induced phase transition of dimethyltetrathiafulvalene-chloranil, a derivative of the widely studied tetrathiafulvalene-chloranil. We then turn attention to tetrathiafulvalene-chloranil itself, investigating the effect of a different external parameter, namely a d.c. electric field, with particular attention to the ferroelectric phase. In the second part of the thesis we shall focus on the problem of polymor-

phism of two important single component organic semiconductors, α-quaterthiophene and rubrene. Polymorphism is an important issue, as it may degrade the device performance. We have attacked the problem through a detailed Raman and computational study of low-frequency, intermolecular phonons, which are very sensitive to the molecular arrangement. The obtained eigenvectors of the intermolecular phonons are the prerequisite for a future investigation of their coupling with the charge carriers.

Part I

Neutral-ionic phase transition

Chapter 1

Mixed stack charge-transfer crystals

1.1 Neutral-ionic phase transition

Strong electron Donor (D) and Acceptor (A) organic π-conjugate1ṃolecules are the building blocks of an important class of materials, the charge-transfer (CT) crystals, which exhibit unusual electrical, optical and magnetic properties. The CT interaction between the D/A frontier orbitals is the origin of the just mentioned unusual properties. In particular, the directional nature of the CT interaction determines the arrangement of the molecules within the crystal, with strong one- or two-dimensional anisotropy (1D or 2D). The most common arrangement is that of a mixed stack (Fig. 1.1), in which D and A molecules pile alternatively face-to-face along one direction, in such a way to favor the overlap between the frontier orbitals. The most evident effect of the CT interaction is the fractional degree of CT (or ionicity, ρ) carried by D and A molecules within the stack. The degree of CT is determined by the competition between two energies: (I-A),the cost of ionizing a donor-acceptor (D-A) pair (I is the ionization potential of the donor and A is the acceptor electron affinity), and E_m, the electrostatic Madelung energy gained if the lattice is ionic. The ground state of the crystal is neutral if $(I - A) > E_m$, and the difference $E_{CT} = (I - A) - E_m$ is the energy necessary to create an ionic pair in neutral lattice. The ground state is ionic if $(I - A) < E_m$, and $E_{CT} = (2\alpha_m - 1)e^2/a - (I - A)$ the excitation energy of a neutral pair within the ionic lattice (α_m is the Madelung constant, and a the DA distance) [1]. If one neglects the CT integral between D and A molecules, the crystal can be either completely neutral, $\rho = 0$, or completely ionic $\rho = 1$. The introduction of the CT between neighboring molecules mixes these two state and makes possible the existence of intermediate value of the molecular charge, namely quasi-neutral or quasi-ionic compounds.

It has been shown that the optical excitation energy $E_{CT} = h\nu_{CT}$ is very well correlated with the $\Delta E_{redox} \sim (I - A)$ of the molecular species, at least for quasi-neutral crystals. Fig. 1.2 shows this correlation for a series of mixed stack CT crystals. The

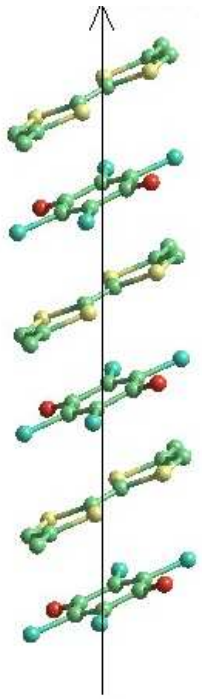

Figure 1.1: Molecules arranged in a mixed-stack.

dotted line indicates the border $\Delta E_{redox} = E_m$ (the Madelung energy is assumed roughly constant for all the crystals), and divides CT crystals in two classes: quasi-neutral and quasi-ionic. From the figure one notices that some compounds are very close to the neutral-ionic border, so that one can think to induce a phase transition by changing an external parameter like pressure or temperature.

The increase in pressure or the decrease in temperature indeed increases the Madelung energy, and may induce the crossing of the $(I - A) = E_m$ borderline, with the passage of the ground state from neutral to ionic. Discovered for the first time in 1981 by J.B.Torrance et al. [1], the so-called neutral-ionic transition made these organic compounds the subject of extensive research [2, 3]. Neutral-ionic transition involve at least two different aspects: a valence or electronic instability and a structural instability. The physical parameters we have to take into account are the electronic charge on the molecular site and the crystal structure, in particular the spatial arrangement and the symmetry of the stacks. Conventionally, the border between neutral and ionic ground state is established at ρ= 0.5. So, crystals having the constituent molecules with a charge less than 0.5 are classified as neutral, and those with molecules with a charge greater than 0.5 are classified as ionic. Neutral crystal generally have regular stack, with equal distances between D and A along the stack. Ionic crystals are instead un-

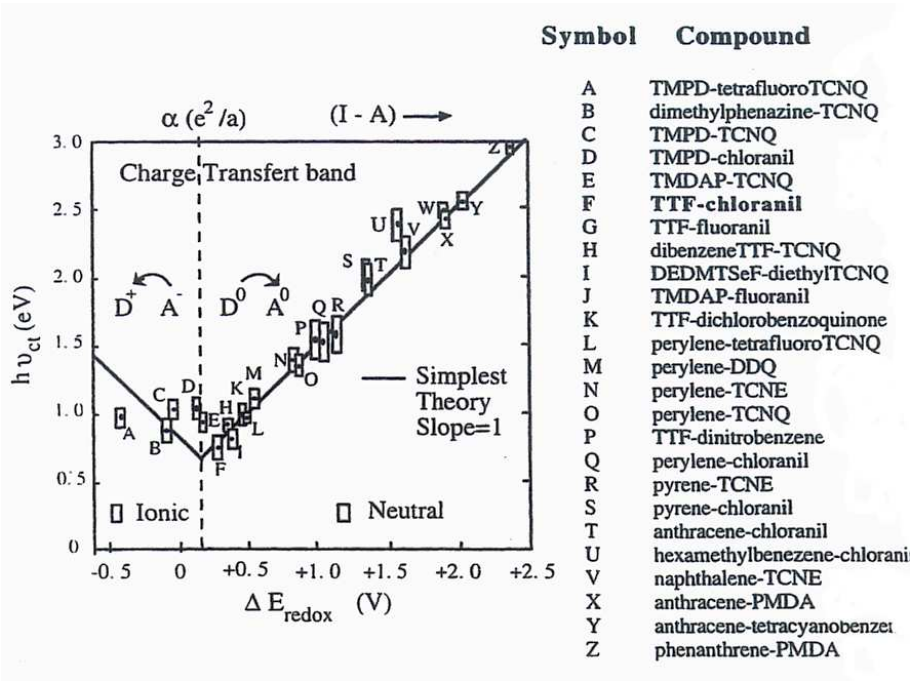

Figure 1.2: Dependence of E_{CT} from ΔE_{redox} (from Ref. [1]).

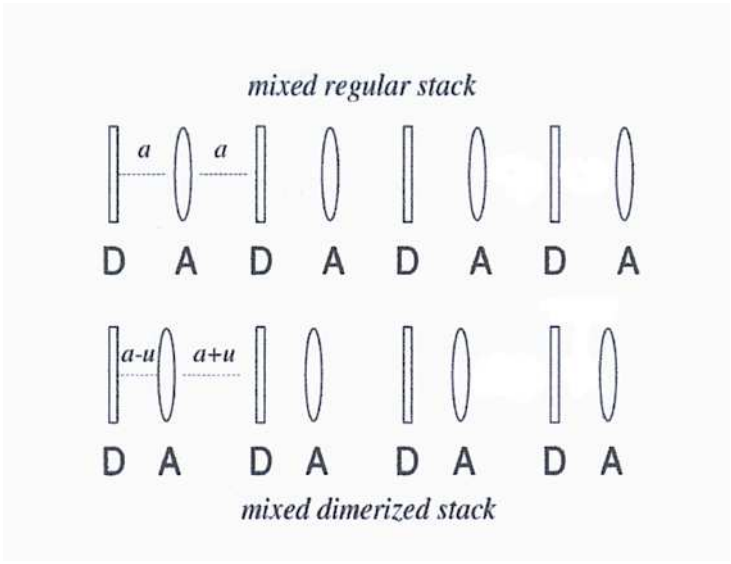

Figure 1.3: Mixed stack compounds: schematic representation of regular (top) and dimerized stack (bottom).

stable towards a dimerization of the stack, with alternating distances between D and A molecules (Peierls instability), the two situations being schematically represented in Fig. 1.3.

1.2 Vibrational spectroscopy of CT crystals

The vibrational modes of organic molecular systems can be approximately divided in intermolecular or lattice modes, having frequencies in the range $\sim 10-120$ cm^{-1}(due to weak intermolecular Van der Waals forces and high molecular mass), and intramolecular modes that involve stretching and bending vibrations of the chemical bonds, and cover a frequency range from approximately 150 to 3000 cm^{-1}.

As an example of the information that can be gathered on the neutral-ionic transition by vibrational spectroscopy in the region of the intramolecular vibrations, we analyze the prototypical mixed stack CT crystal tetrathiafulvalene-chloranil (TTF-CA), which has been the object of extensive studies. The equilibrium geometry of the examined

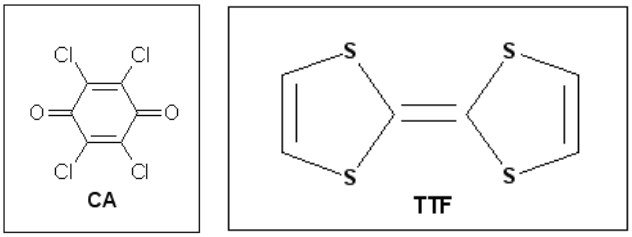

Figure 1.4: Chloranil (CA) and tetrathiafulvalene (TTF) molecules.

molecules is reported in Fig. 1.4. Both molecules have a high number of vibrational degrees of freedom, but are also highly symmetric, so a symmetry analysis helps to interpret the vibrational spectra. For instance, both molecules have a center of symmetry, so that the vibrations are symmetric or antisymmetric (*gerade* and *ungerade*) with respect to the center. In this situation the mutual exclusions rule holds, and *ungerade* modes are active only in infrared (IR), whereas *gerade* modes are only Raman active. IR and Raman spectroscopies then become complementary techniques.

By using the full D_{2h} symmetry of the CA and TTF molecules we obtain the following classification and vibrational activity of the molecular modes:

- for the chloranil molecule

$$\Gamma_{vib} = 6a_g + b_{1g} + 3b_{2g} + 5b_{3g} + 2a_u + 5b_{1u} + 5b_{2u} + 3b_{3u} \tag{1.1}$$

- for the tetrathiafulvalene molecule

$$\Gamma_{vib} = 7a_g + 2b_{1g} + 3b_{2g} + 6b_{3g} + 3a_u + 6b_{1u} + 6b_{2u} + 3b_{3u} \tag{1.2}$$

The a_g, b_{3g}, b_{1u} and b_{3u} are vibrations in the molecular plane, and the b_{1g}, b_{2g}, a_u, and b_{3u} are out of plane vibrations. The *ungerade* vibrations, except a_u, are IR active, whereas all the *gerade* vibrations are Raman-active.

Thus one can easily predict the number of vibrations present in the optical spectra. The analysis refers to the molecules in the gas phase and in a real crystal the number of active-vibrations can be modified if the molecular site symmetry in the solid is different. In addition, due to intermolecular interactions, one can observe the coupling between vibrations on different molecular sites within the unit cell, and consequently the splitting of the otherwise degenerate energy levels.

Polarized spectra on single crystal help in the assignment on the modes to the different symmetries. The light propagates in the crystal along proper extinction directions, and in a mixed-stack crystal one of these directions coincide with the stack direction, and the other two are orthogonal to it. As an example we report the infrared spectra of TTF-CA for the face containing the stack axis, with polarization parallel and perpendicular to the stack.

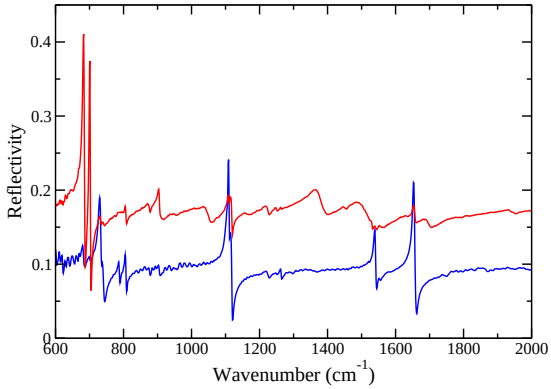

Figure 1.5: Reflectivity spectra polarized parallel (red-line) and perpendicular to the stack axis (blue-line) in TTF-CA.

In this context we are not interested to a complete vibrational assignment and we limit to describe the most important features. Keeping in mind the stack structure in Fig. 1.1, it is clear that in the polarization perpendicular to the stack axis one observes the in-plane vibrations. The most intense bands are attributed to the C=O, C=C, C-Cl stretching vibrations of the chloranil molecule (approximately at 1650, 1530, and 1100 cm^{-1}, respectively). In the polarization parallel to the stack axis out-of-plane molecular vibrations are present. They are bending vibrations, and occur below about 800 cm^{-1}, the higher frequency region being almost completely flat.

Now we want to study the effect of the CT interaction in the optical spectra of these mixed-stack compounds. Fig. 1.6 reports the reflectivity spectra of TTF-CA up

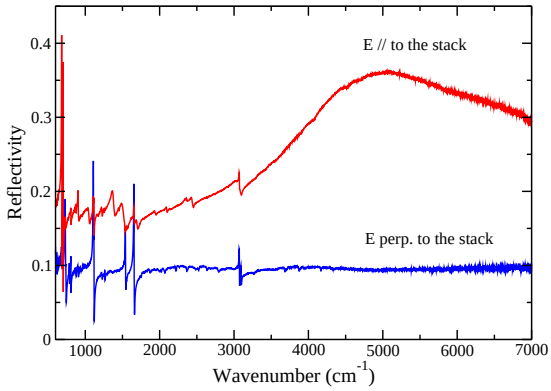

Figure 1.6: Reflectivity along the stack axis (red-line) and perpendicular to it (blue-line) for mixed-stack TTF-CA.

to 7000 cm^{-1}. In the polarization parallel to the stack one observes a broad feature that extends from 3000 to 7000 cm^{-1}. This band has an electronic origin, and is due to the CT excitation. The presence of this electronic excitation is peculiar of the CT compounds, and for mixed stack CT crystals close to the neutral-ionic borderline like TTF-CA, it occurs at low frequency, in the near-IR region of the spectra (cf. Fig. 1.2). As a consequence, it has strong effects on the vibrational levels. The coupling between the CT excitation and the intramolecular vibrations (e-mv coupling) and its effects on the optical spectra of 1D CT crystals have been extensively treated in the context of different theoretical framework [4, 5]. For the aim of the present discussion we can

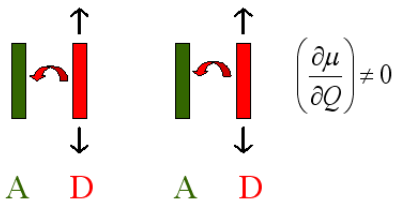

Figure 1.7: Charge transfer in a dimer induced by a totally symmetric vibration.

consider a schematic model of one D and one A molecule and their frontier orbitals. The totally symmetric (a_g) vibrations are the only ones that modulate the HOMO and LUMO energies. Therefore they also modulate the charge transfer that involve the HOMO and LUMO orbitals. In this way vibrational and electronic energy states are mixed, giving rise to the so-called vibronic states. The a_g vibrational frequencies are therefore perturbed (lowered) with respect to the frequency one would observe if the CT excitation were moved to infinite energy.

The a_g vibrations are therefore coupled to the CT transition, and as such they can be used as a structural tool. As discussed in the previous Section, in mixed stack CT crystals the stack can be either regular or dimerized. In the regular stack all the molecules are equidistant, and therefore reside on inversion center within the crystal. In the dimerized stack DA dimers are formed, and the inversion center on the molecule is lost. As a consequence, in a regular stack, the a_g molecular modes are Raman-active only, whereas in a dimerized stack they become both Raman and IR active, obviously at the same frequency. Therefore the activation of a_g modes in the IR spectra is the signature of a dimerized stack. As discussed above, the a_g molecular modes are coupled to the CT electrons, and in the dimerized stack they borrow intensity from the nearby CT transition. They therefore are highly intense in the IR spectra with polarization parallel to the stack axis, namely in the direction of the CT transition. The a_g molecular modes are in-plane vibrations, but if the stack is dimerized they dominate the spectrum with polarization *perpendicular* to the molecular plane, and are easily identified. The activation of the a_g modes is therefore the most evident spectroscopic change induced by the dimerization, and represents the basis of its spectroscopic determination.

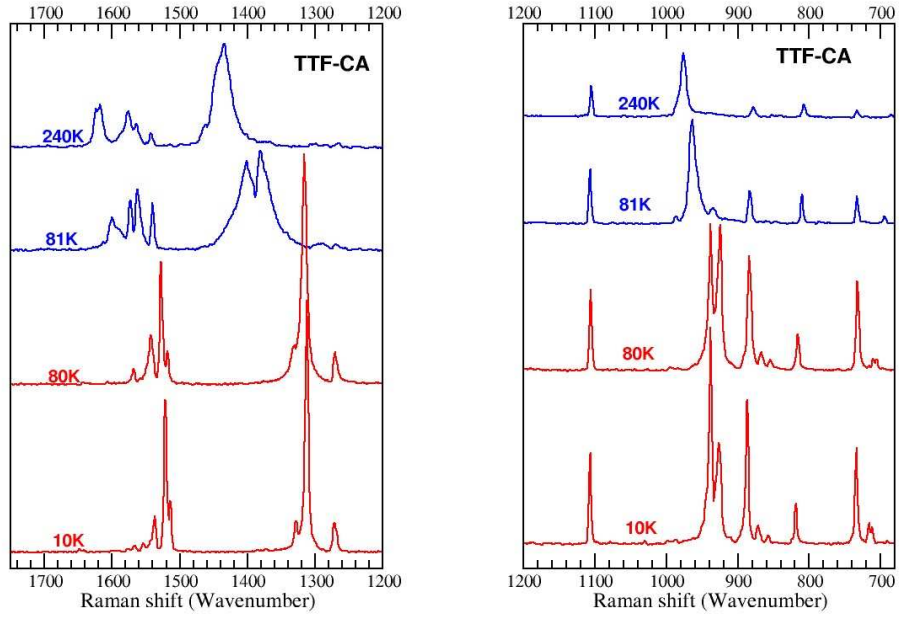

Figure 1.8: Temperature dependence of a_g modes of TTF-CA.

As an example we report the behavior of two a_g modes for TTF-CA that undergoes the neutral-ionic transition at 81 K. On the neutral side, the stack is regular, and in

the ionic phase it dimerizes. Fig. 1.8 shows the a_g modes around 980 and 1440 cm^{-1}. Their frequencies are perturbed by the interaction with the CT excitation and are very sensitive to the change in the electronic parameters as the temperature is varied. As a consequence, their frequency is *lowered* by lowering temperature, opposite to the normal behavior, and have a large anomalous shift compared to the other modes.

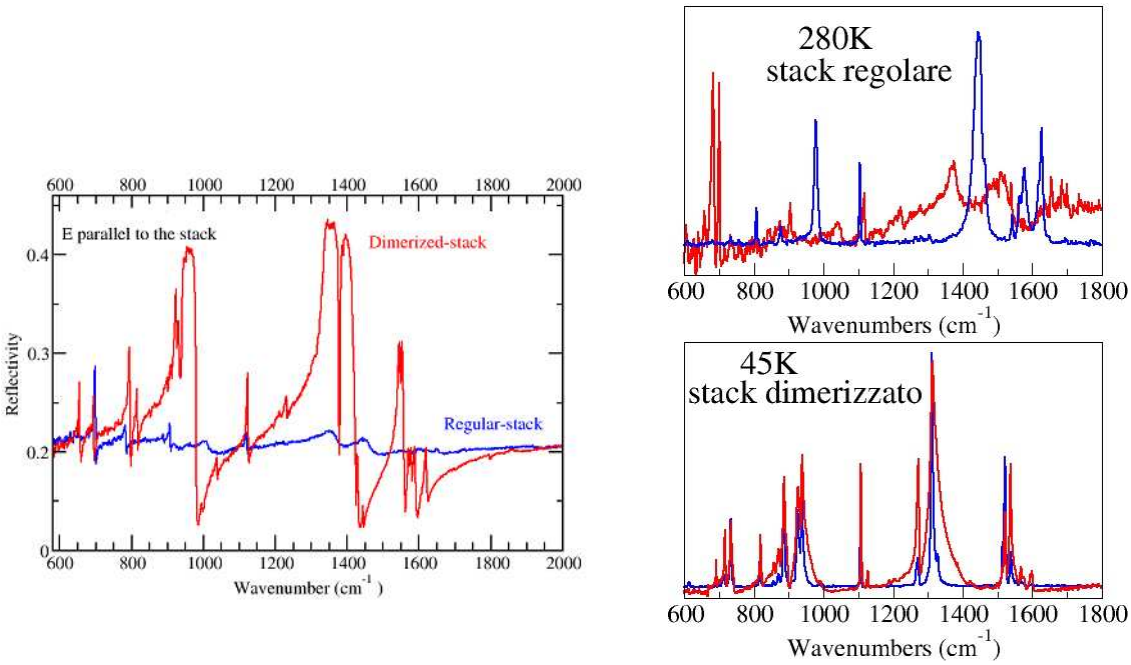

Figure 1.9: Activation of a_g modes (left) and Raman-infrared coincidence (right) in the dimerized phase of TTF-CA.

From the IR spectra polarized along the stack axis we can see when the vibronic bands become active. Fig. 1.9 shows the comparison between reflectivity polarized along the a stack axis in the high-temperature centro-symmetric phase (blue line) and in the low-temperature non-centro-symmetric phase (red-line). It is evident the activation of the a_g modes having a giant intensity around 950, 1350, 1550 cm^{-1}. Moreover, in the dimerized phase, the frequencies of the vibronic bands are the same both in Raman and infrared spectra, as it can be easily checked in Fig. 1.9.

Neutral-ionic phase transition imply the dimerization of the stack, as we have just seen, but also a change of the ionicity ρ across the neutral-ionic borderline ($\rho = 0.5$) Vibrational spectroscopy also offers an easy way to determine this parameter. The frequencies of the molecular vibrations are indeed sensitive to the degree of the molecular charge, and in general one can assume a linear dependence of the frequency from ρ.

However, for most modes the induced frequency change is not large enough to allow a determination of this value with a sufficient accuracy. In addition, the linear relationship holds in the absence of the e-mv coupling. Therefore for a mixed stack CT crystal the a_g modes cannot be used to estimate ρ, since their frequency is affected by the molecular charge *and* by the coupling with the CT transition [4]. The latter contribution cannot be easily separated, although in some case this has been done [5]. As a consequence to evaluate ρ we need to consider molecular vibrations that are not affected by the e-mv coupling, and in the IR spectra these can be found in the polarization perpendicular to the stack axis, where the e-mv coupling has no effect.

In the case of TTF-CA, the first measurements and calculations [6] showed that the vibration most sensitive to ρ is the antisymmetric b_{1u} carbonyl stretching of the chloranil molecule. This mode, which has a ionization frequency shift of 160 cm^{-1}, is the one usually preferred to estimate the ionicity of CT crystals in which chloranil is involved. As a part of the work of the present thesis, we have recently shown that also the the C=C antisymmetric stretching vibration of the chloranil molecule can be profitably used to deduce the ionicity [7]. The C=C stretching frequency depends linearly from ρ, but has an infrared intensity detectable only for $\rho \lesssim 0.5$, namely, on the neutral side. The linear dependence of the C=O and C=C frequencies from ρ has been experimentally tested (Fig. 1.10), and the quantitative dependence is given by:

$$\nu_{C=O} = 1685 - 160\rho \tag{1.3}$$

$$\nu_{C=C} = 1566 - 116\rho \tag{1.4}$$

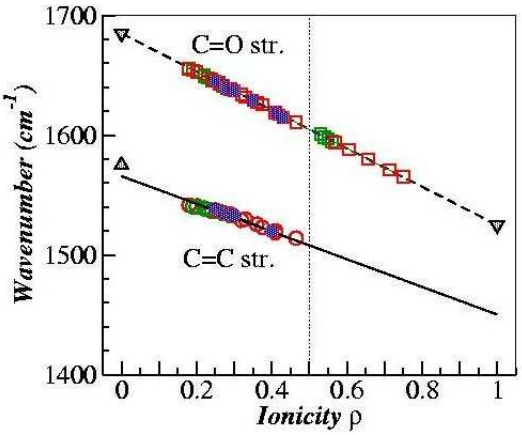

Figure 1.10: Ionicity dependence of the frequency of C=O (squares) and C=C (circles) antisymmetric stretching in CA. Triangles label the frequencies of fully neutral and fully ionic molecule.

Chapter 2

Temperature induced phase-transition in DmTTF-CA

2.1 Aim of the work

As discussed in the previous chapter, a few mixed stack CT salts have N-I and Peierls transition, in which ϱ changes rapidly and the regular stack dimerizes, yielding a potentially ferroelectric ground state [8]. N-I transitions are thus valence instabilities implying a *collective* CT between D and A sites, and as such are accompanied by many intriguing phenomena, such as dielectric constant anomalies, current-induced resistance switching, relaxor ferroelectricity, and so on [9]. The prototypical and most studied compound exhibiting N-I transition is tetrathiafulvalene-chloranil (TTF-CA). The isostructural series formed by 4,4'-dimethyltetrathiafulvalene (DmTTF) with substituted CAs, in which one or more chlorine atom is replaced by a bromine atom, is also interesting. In this case, in fact, the transition temperature and related anomalies can be lowered towards zero by chemical or physical pressure, attaining the conditions of a quantum phase transition [10, 11, 12].

Albeit several aspects of the N-I transition in Br substituted DmTTF-CA family are worth further studies, in the present thesis we shall limit attention to the pristine compound, DmTTF-CA. Despite intensive studies [10, 11, 12, 13, 14, 15], the transition still presents controversial aspects. Through visible reflectance spectra of single crystals and absorption spectra of the powders, Aoki [13] suggested that by lowering the temperature below 65 K, DMTTF-CA does not undergo a full N-I transition, but forms a phase in which both N ($\varrho = 0.3 - 0.4$) and I ($\varrho = 0.6 - 0.7$) species are present. The structural investigation as a function of temperature [14] put in evidence a fundamental aspect of the transition, only implicit in Aoki's work [13]: At 65 K the unit cell doubles along the c axis (a is the stack axis). The order parameter of the transition, which is second-order, is the cell doubling coupled with the dimerization [14]. So above 65 K

the cell contains one stack, and at 40 K contains two stacks, both dimerized, and inequivalent (space group $P1$). From the bond distances, ϱ is estimated at 0.3 and 0.7-0.8 for the two stacks, respectively [14]. In this view, and considering that the two stacks are dimerized in anti-phase, at low temperature DMTTF-CA has a *ferrielectric* ground state.

However, the above scenario has been questioned [10, 11, 16]. Polarized single crystal infrared (IR) reflectance measurements suggests that N and I stacks do not coexist. Only one ionicity is observed, changing continuously from about 0.25 at room temperature to about 0.48 at 10 K, the maximum slope in the $\varrho(T)$ occurring around 65 K. The crystal structure at 14 K indicates a $P\bar{1}$ space group, with two equivalent, dimerized stacks in the unit cell, and *anti-ferroelectric* ground state [11]. According to this picture, the mechanism of DmTTF-CA phase transition is very similar to the other N-I transitions [8, 9]. The Madelung energy change yields an appreciable change of ϱ (about 0.1) within a few degrees of temperature, accompanied by a stack dimerization. The cell doubling appears to be a secondary aspect, whereas the most important feature is the continuous variation of ϱ, as opposed for instance to the discontinuous, first order transition of TTF-CA [8].

Some questions remain however unanswered in the above picture [10, 11]. The transition displays a continuous ionicity change with T, and consequently one would expect huge anomalies at the transition, whereas for instance the dielectric constant increase at T_c is less than in the case of TTF-CA [8, 9]. Furthermore, what is the driving force of the transition? In TTF-CA, the N-I transition is attributed to the increase of Madelung energy by the lattice contraction [1]. If it is so also for DmTTF-CA, what is the role of cell doubling? Finally, although $P1$ and $P\bar{1}$ space groups are sometimes difficult to disentangle by X-ray diffraction, the issue of the different published structures is not solved, both exhibiting good confidence factors in the refinement process [11, 14].

In order to clarify these open questions, and to understand the mechanism of the phase transition in DmTTF-CA, we have decided to collect and re-analyze complete polarized IR and Raman spectra of DmTTF-CA single crystals, along the same lines followed for TTF-CA [17, 18, 19]. Indeed, a careful analysis can give information about ϱ, stack dimerization, and the Peierls mode(s) inducing it. Vibrational spectra give information about the *local* structure, and from this point of view are complementary to the X-ray analysis, which probes long range order. We shall show that DmTTF-CA transition can hardly be classified as a N-I transition, the most important aspect being the stack dimerization and cell doubling. We shall also offer some clues about the origin of the discrepancies in the two X-ray determinations [11, 14].

2.2 Experimental

DmTTF-CA single crystals have been provided by Dr. M. H. Lemée-Cailleau (ILL, Grenoble), and have been prepared as previously described [14]. The IR spectra (600-8000 cm^{-1}) have obtained with a Bruker IFS66 FTIR spectrometer, equipped with A590 microscope. Raman spectra have been recorded with a Renishaw 1000 micro-spectrometer. The excitation of Raman has been achieved with a Lexel Krypton laser ($\lambda = 647.1$ nm), backscattering geometry, with less than 1 mW power to avoid sample heating. A pre-monochromator has been used for the low-frequency spectra (below 200 cm^{-1}). For the high frequency Raman spectra we report only the spectra obtained for incident and scattered light both polarized perpendicularly to the stack axis, ($\perp\perp$) in the conventional notation. In this arrangement the in-plane molecular modes, notably the totally symmetric ones, are more clearly visible. The spectral resolution of IR and Raman spectra is 2 cm^{-1}.

Temperatures down to 10 K have been reached with a ARS closed-circle cryostat, fitted under the IR and Raman microscopes. The temperature reading on the cold finger has been tested and considered accurate to ± 2 K for the Raman and IR reflectance measurement, where silver paste has been used to glue the sample to the cold finger. For IR absorption the temperature reading is far less accurate, due to the imperfect thermal contact between the sample and the KBr window on the cold finger. Temperature reading corrections have been applied based on the comparison with the reflectivity data. DmTTF-CA reflectivity has been normalized to that of an Al mirror, without further corrections. Therefore the reflectance values are not absolute, and relative values can be compared with confidence only within each low-temperature run. We consider reflectance values of the spectra below 20 K not reliable in any case, because the deposition of an unknown contaminant on the DmTTF-CA surface introduces high noise above ~ 2000 cm^{-1}.

2.3 Valence instability

The first question we address is that of the ionicity as a function of temperature. To such aim, we have collected both IR reflectance and absorbance spectra, with polarization perpendicular to the stack axis. The two types of spectra allow us to ascertain whether probing the surface or the bulk yields the same result. Unfortunately, we were unable to obtain crystals sufficiently thin to avoid saturation of the most intense absorption bands, so the information provided by the two types of spectra are complementary. Fig. 2.1 shows some examples of spectra as a function of temperature in the frequency range 1500-1700 cm^{-1}. The two structures at 1649 $cm^{-1}$and 1539 cm^{-1}(at 150 K) are assigned to the $b_{1u}\nu_{10}$ and $b_{2u}\nu_{18}$ modes of the CA moiety, corresponding to the C=O and C=C antisymmetric stretching vibrations, respectively [17]. The C=O stretching

mode is the most sensitive to the molecular charge, so it has been almost invariably used to estimate the ionicity. However, recent investigations on CA and CA^- molecular vibrations have shown that also the C=C mode should be a good ϱ indicator [7, 20]. Therefore we shall use C=O $b_{1u}\nu_{10}$ as a primary ϱ indicator, and C=C $b_{2u}\nu_{18}$ mode as secondary, internal consistency probe.

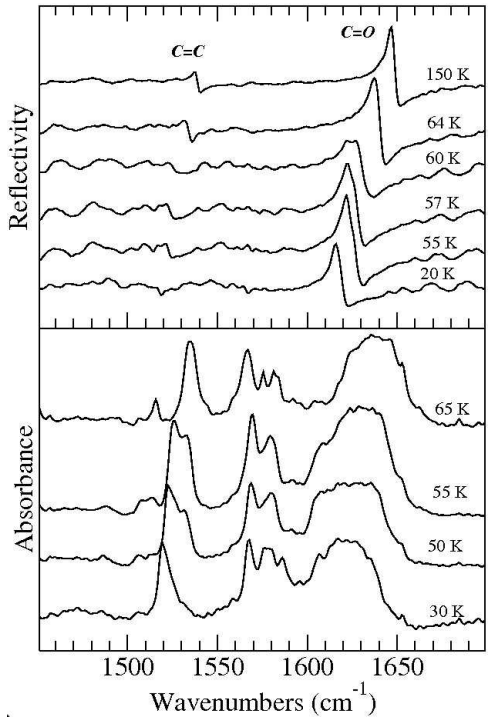

Figure 2.1: Temperature evolution of DmTTF-CA reflectance and absorbance spectra, polarized perpendicularly to the stack. The bands corresponding to C=O and C=C stretching of CA are marked.

As the C=O stretching mode saturates in absorption (Fig. 2.1, bottom panel), we have performed the usual Kramers-Kronig transformation of the reflectance spectra.

From the frequency reading of the C=O $b_{1u}\nu_{10}$ mode we have estimated the ionicity by the usual relationship:

$$\rho = (\bar{\nu}(0) - \bar{\nu}_{exp}(C=O))/\Delta_{ion} \tag{2.1}$$

where $\bar{\nu}(0)$ is the C=O stretching frequency of the neutral molecule and Δ_{ion} is the ionization frequency shift. The temperature evolution of ρ is reported in Fig. 2.2. The charge slowly increases as the temperature is lowered down to about 65 K. A rapid change occurs from 65 to approximately 40 K, where the ρ value has almost attained the

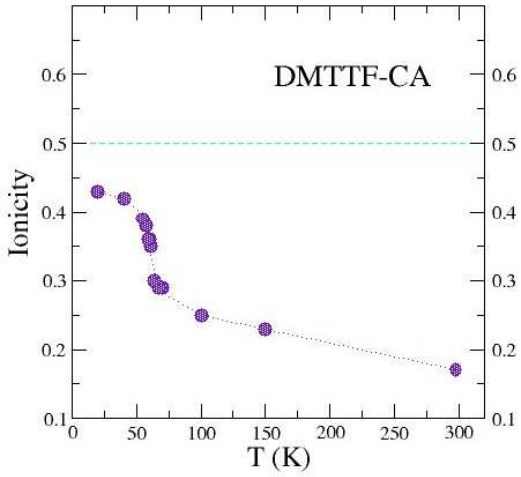

Figure 2.2: Temperature dependence of ionicity of DmTTF-CA estimated from the frequency of the C=O stetch mode.

lowest temperature (10 K) value. No discontinuous changes but just gradual variations are evident. At 10 K the value of the ionicity does not overcome the conventional neutral-ionic borderline ($\rho = 0.5$), so DmTTF-CA always remains in the neutral state.

An important difference of our results compared with those present in the literature [10] is that just below the phase transition temperature, between 62 and 54 K, the C=O stretching mode shows a clear doublet structure (Fig. 2.1, top panel), suggesting the presence of two slightly differently charged molecular species. The indication is confirmed by the band due to the C=C stretching mode, which also shows a doublet structure, clearly seen in absorption (bottom panel of Fig. 2.1). The frequency (and ionicity) difference is small, but clearly visible irrespectively of the direction of temperature change, and reproducible in different runs. Actually, a hint of a doublet structure is visible also in Ref. [10] spectra, but it was interpreted as a band broadening.

To summarize, our results present a valence instability scenario different from both the previously reported ones [10, 13]. The ionicity change appears to be continuous across the phase transition. The crystal remains neutral ($\rho \sim 0.43$ at 20 K), therefore excluding the simple term of N-I transition: it is better to refer to it as a valence instability. Finally, in a temperature interval of less than 10 K below 65 K there is coexistence of two species with slightly different molecular ionicity, both on the neutral side, with $\rho \sim 0.36$ and 0.38.

2.4 Dimerization instability

The stack dimerization implies a change in the symmetry of the system, namely, the loss of the inversion center located on the molecular sites of a regular stack. Due to the lack of this symmetry element, the molecular totally-symmetric Raman-active modes also become IR-active in the polarization parallel to the stack axis [17]. Due to their coupling to the electronic CT transition, these "vibronic" states acquire high spectral intensity and can be easily identified. In Fig. 2.3 we report the reflectivity spectra polarized along

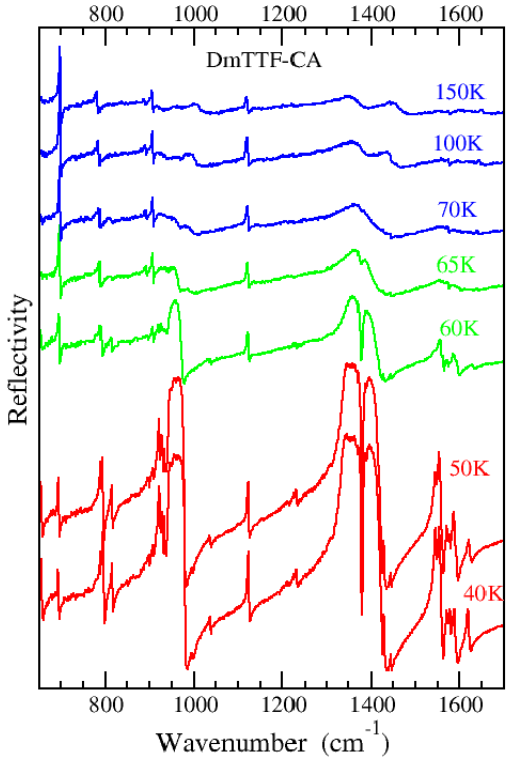

Figure 2.3: Temperature dependence of DmTTF-CA reflectivity spectra polarized along the stack above and below the phase transition. The spectra are y-shifted for the sake of clarity.

the a stack axis above and below the transition temperature. Totally-symmetric (a_g) modes are clearly visible at about 950 and 1350 cm^{-1}. These modes are attributed to the breathing mode of the chloranil molecule and to the C=C stretching mode of DmTTF moiety, respectively. Below 65 K the presence of a dip structure in this last band, below 65 K, is due to the interference effect of a weak band superimposed to the C=C vibration frequency. In the low-temperature phase the intensity of a_g activated modes grows by decreasing temperature, as evidenced in Fig. 2.4. The intensity (oscillator strength) of

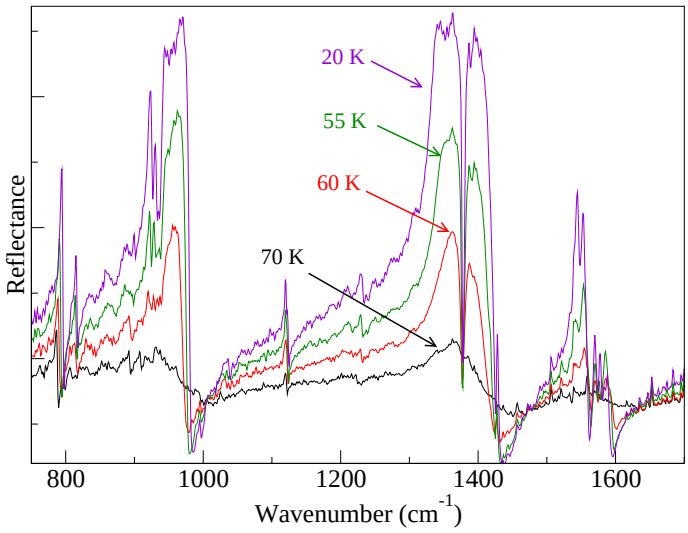

Figure 2.4: Temperature dependence of DmTTF-CA reflectivity spectra polarized along the stack. The reflectance scale is not reported, as only relative reflectance values can be trusted.

the vibronic bands is related to the dimerization amplitude [21]. The relationship is not of direct proportionality, but in any case the intensity gives an indication of the increase of the dimerization amplitude at the transition. The oscillator strength of the above a_g modes as a function of T is extracted by fitting the reflectance spectra with a Drude-Lorentz oscillator model, where the dielectric constant is given by:

$$\epsilon(\omega) = \epsilon_\infty + \sum_j \frac{f_j}{{\omega_j}^2 - \omega^2 - i\omega\gamma_j} \tag{2.2}$$

where ϵ_∞ is the high-frequency dielectric constant, f_j is the oscillator strength, and γ_j is the linewidth.

The temperature dependence of f_j for the two modes, normalized to the 20 K value, is reported in the middle panel of Fig. 2.5. It is zero in the high-temperature phase and it increases below the critical temperature, displaying a behavior typical of an order parameter relevant to a second-order phase transition. It is instructive from this point of view to compare the present data with the intensity of the X-ray diffraction spots related to the cell doubling, as reported in Ref. [14] and shown in the bottom panel of Fig. 2.5. The two sets of data exhibit the same behavior, demonstrating that the cell doubling, as detected by X-ray, and stack dimerization amplitude, as detected by IR spectra, occur at the same time, representing two inseparable aspects of DmTTF-CA phase transition.

Close scrutiny of the three panels in Fig. 2.5, which compare the valence and dimerization instability, suggests that the valence instability *follows* the structural modification. Dimerization and cell doubling start at $T_c \simeq 65$ K, whereas the $\varrho(T)$ curve presents the maximum slope around 62 K, after which the simultaneous presence of species with two slightly different ionicities is detected.

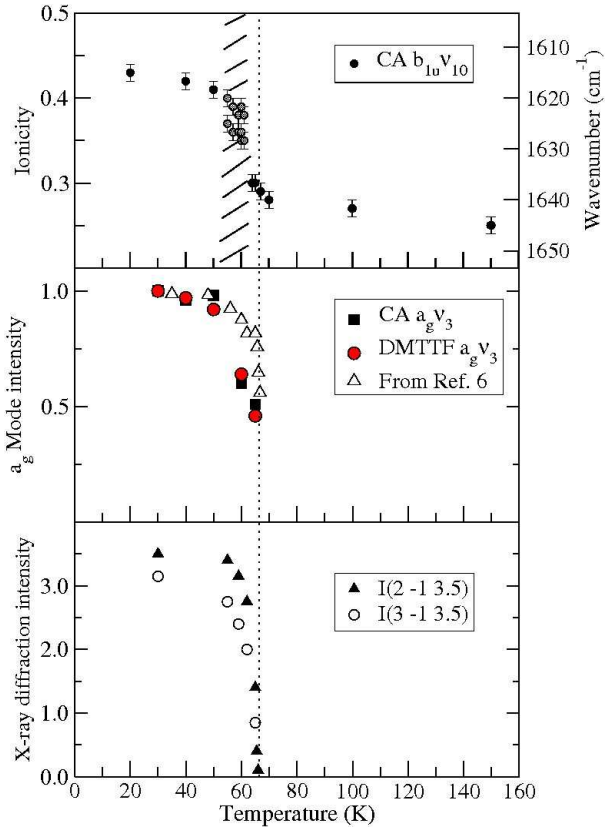

Figure 2.5: Temperature evolution of three DmTTF-CA observable. Top panel: Ionicity ρ. The yellow shaded area indicates the temperature interval in which two slightly different ionicities are observed. Middle panel: Normalized intensity of IR vibronic bands, connected to the stack dimerization amplitude. Bottom panel: Intensity of X-ray reflections signaling the cell doubling (from Ref.[14]). The vertical dashed line marks the critical temperature $T_c \approx 65K$.

2.5 Soft-mode and dielectric properties

In the dimerized low-temperature phase the lack of the inversion center on the stack and the increase of the molecular charge yields to the formation of electric dipole moments. Their arrangement in the stack and among the stacks defines the presence of a macroscopic local polarizations. From dielectric constant measurements the variation of the electric properties during the phase transition are clearly visible. The temperature

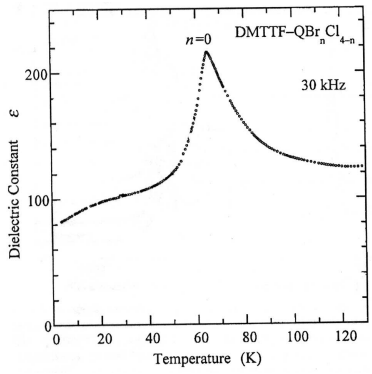

Figure 2.6: Dielectric constant of DmTTF-CA as a function of temperature.

evolution of the dielectric constant in DmTTF-CA is reported in Fig. 2.6. Its temperature behavior clearly show the presence of a dielectric anomaly in concomitance with the electronic and structural phase-transition as described in the last paragraphs.

This curve is similar to that observed in the widely studied inorganic ferroelectric compounds, like titanates or niobates. These compounds are made up of ionic TiO_3 or NbO_3 units and Ba, Sr, Li or K cations, and by lowering temperature undergo structural phase transition with asymmetric displacement of metal atom in the anionic covalent unit. As a consequence, we have the generation of a cell dipole moment below the transition Curie temperature. These dipole moments are usually arranged in a ferroelectric disposition, giving rise to a polarized local domains. As the close relationship between atomic displacements and dielectric properties was discovered, it was natural to look at the origin of the dielectric anomaly in terms of the lattice dynamics, yielding the so-called soft-mode theory. The dielectric constant is related to the vibrational frequencies of the lattice through the Lyddane-Sachs-Teller (LST) equation:

$$\frac{\epsilon_0}{\epsilon_\infty} = \prod_j \frac{(\omega_{j,LO})^2}{(\omega_{j,TO})^2} \tag{2.3}$$

In the high-temperature, para-electric phase, the Curie law applies:

$$\epsilon = \epsilon_\infty + \frac{4\pi}{T - T_c}, \tag{2.4}$$

and if we exclude the possibility that $\omega_{LO} \to \infty$ when $T \to T_c$, the Curie law implies a square root temperature dependence of the frequency of one vibrational mode:

$$\omega_{TO} \propto \sqrt{T - T_c} \tag{2.5}$$

The identification of a vibrational mode following this temperature law is the demonstration of the intrinsic instability of the lattice towards a structural deformation and gives insight about the mechanism of the transition. As an example we want to cite the work on $KNbO_3$ [22]. Fig. 2.7 shows the reflectivity at different temperatures and the imaginary part of the frequency-dependent dielectric constant as calculated from reflectivity by means of Kramers-Kronig analysis. The complete series of reflectivity measurements extended to the far IR region evidences the existence of an high-intensity low frequency mode, whose frequency shifts toward zero as the temperature approaches the Curie critical temperature.

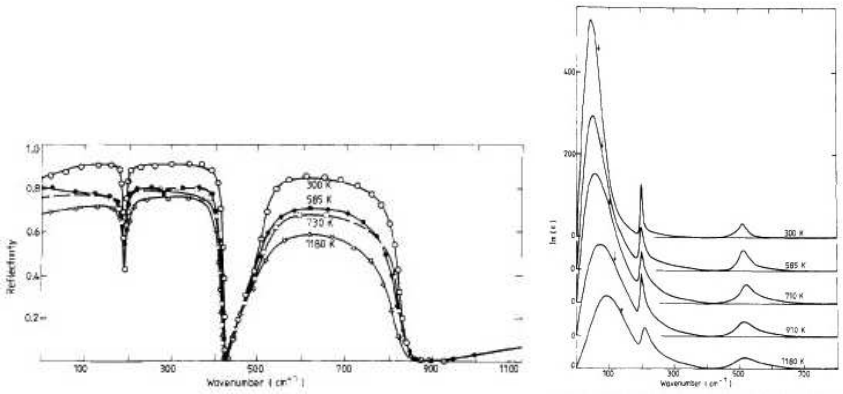

Figure 2.7: Left: Infrared reflectivity spectra of $KNbO_3$ as a function of temperature. Right: Temperature dependence of the imaginary part of the dielectric function as obtained from the Kramers-Kronig analysis.

The neutral-ionic phase transitions are accompanied by a growth of the dielectric constant that rapidly decreases after the critical temperature, as exemplified in Fig. 2.6. The arrangements of the dipole moments in adjacent dimerized stacks in the low temperature phase can be ferroelectric, as in the case of TTF-CA, or anti-ferroelectric, as in the case of DmTTF-CA. The origin of the stack dimerization in these quasi-one dimensional crystals can be ascribed to the Peierls instability. Mixed-stack organic systems are not metals and the ionic phase can not be considered as a chain of ionic molecules carrying a spin $S = 1/2$ because molecules are not completely ionized. A pure Peierls-mechanism or a spin-Peierls one does not apply for the neutral-ionic transition: we have a generalized Peierls instability involving both electronic and spin degrees of freedom.

The Peierls instability is due to the coupling of the lattice, inter-molecular phonons to the electronic system, and the implied Peierls phonons have a soft behavior.

The phase transition of DmTTF-CA is a complex one, implying both the stack dimerization (along the a axis) and a cell doubling perpendicularly to the stack, along the c^* axis. Therefore it should imply the occurrence of soft phonon(s) yielding the stack dimerization and the cell doubling. In a simplified but effective view, we can think of the phase transition as due to just one critical phonon, with wavevector $c^*/2$. Such a phonon belongs to a phonon branch that corresponds to stack dimerization along the a stack axis, and at the zone-center is optically active. In other words, the cell doubling can be ascribed to the effect of an anti-phase vibration along the c-axis. The driving force of the transition is then provided by the Peierls mechanism, which couples the zone-center dimerization mode, i.e., the Peierls mode, with the CT electronic structure [23]. The electron-phonon coupling causes the softening of the Peierls mode, eventually leading to stack dimerization. However, in the proximity of the phase transition, where interstack interactions are more effective [15], the Peierls mode evolves to a stack dimerization out-of-phase in nearest-neighbors cells, when it softens yielding the cell doubling along the crystallographic direction c. Of course, in the complicated phonon structure of a molecular crystal like DmTTF-CA, the Peierls mode may result from the superposition (mixing) of several phonons, all directed along the stack. A spectroscopic investigation of DmTTF-CA, along the lines already developed for TTF-CA [18, 19], should yield the identification of these phonons or of the resulting "effective" Peierls mode.

Phonons coupled to the CT electrons along the chain are most likely inter-molecular, or lattice, phonons [19]. We start by classifying the lattice phonons and their Raman and IR activity by adopting the rigid molecule approximation, which separates the inter-molecular from the intra-molecular phonons. Then, in the high temperature (HT) phase ($P\bar{1}, Z = 1$)[14] we expect 9 optically active lattice modes, $6A_g(\mathcal{R})+3A_u(\mathcal{T})$. The Raman active A_g modes can be described as molecular librations ($\mathcal{R}$), and are decoupled from the CT electrons. Coupling is instead possible for the IR active A_u phonons, which indeed correspond to translations ($\mathcal{T}$). There are no symmetry constraint about the direction of molecular displacements, so we may have some component of all the three A_u phonons along the stack axis, contributing to the Peierls mode.

In the low-temperature (LT) phase it is not clear if the two stacks inside the unit cell are inequivalent, with space group $P1$ [14], or equivalent, with space group $P\bar{1}$ [11]. Since in any case the inequivalence is small, for the spectral predictions we find more convenient to use the centro-symmetric description. The center of inversion is between the two stacks in the unit cell, then we expect 21 optically active modes, $12A_g(6\mathcal{T}+6\mathcal{R})$ and $9A_u(6\mathcal{R}+3\mathcal{T})$. Therefore, the phonons modulating the CT integral are IR active in both HT and LT phases, whereas the cell doubling in the LT phase makes Raman active 6 translational phonons, which correspond to the coupled in-phase displacements of the two chains.

In the HT-phase the Peierls lattice phonons are IR-active, and occur in the far-infared

region of the spectrum (10-150 cm^{-1}). Direct investigation of the Peierls phonons in the HT phase is not easy, due to the low reflectivity of these insulator compounds and the low-sensitivity of normal spectrometers in this spectral region. However, as reported for the case of TTF-CA [18], the soft mode may appear as a combination mode in the mid-IR region of the spectrum. Therefore we now compare the mid-IR spectra with polarization parallel to the stack axis with the Raman spectra collected at the same temperatures.

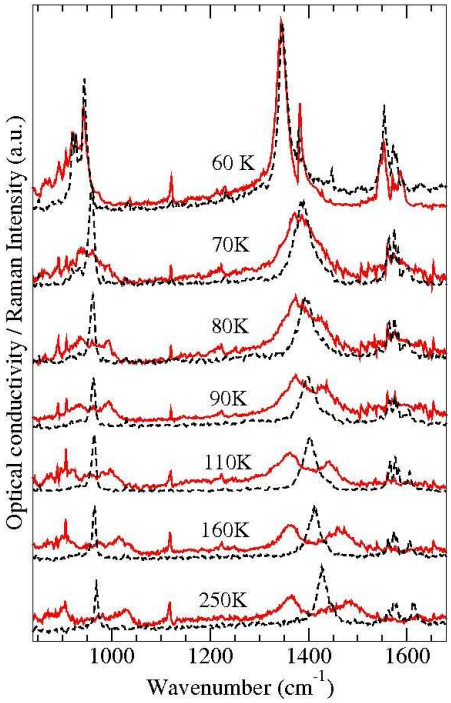

Figure 2.8: Temperature dependence of DmTTF-CA Raman spectra (black, dashed line), and IR conductivity spectra polarized parallel to the stack axis (red, continuous line).

Examples of the spectra above the transition temperature are reported in Fig. 2.8. The IR spectra above 80 K exhibit pairs of absorptions ("side-bands") that approach each other when the temperature is lowered, eventually coalescing at the transition. On the other hand, the Raman-active a_g modes, coupled to the CT electrons, are located exactly between the IR "side-bands", as exemplified by the Raman bands located at about 960 and 1430 cm^{-1}. Therefore IR side-bands are interpreted as combination modes between the intra-molecular a_g band and a lattice phonon. In the top panel of Fig. 2.9, the frequency difference between the Raman band and the corresponding IR side-bands is plotted as a function of the temperature. The soft behavior showed by

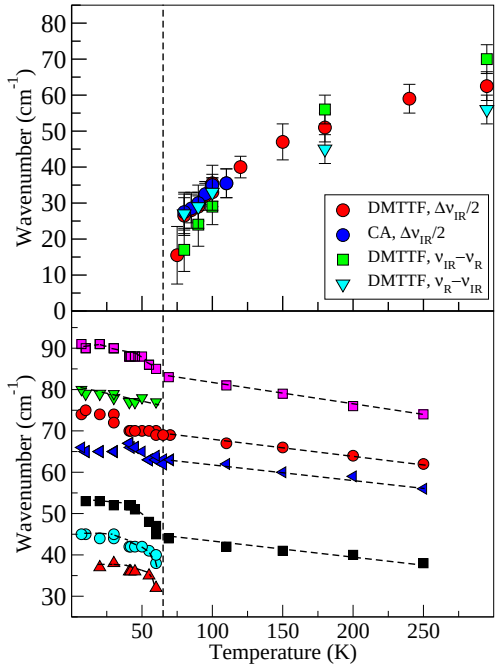

Figure 2.9: Top panel: Frequency difference between Raman DmTTF $a_g\nu_3$ and CA $a_g\nu_3$ bands and the corresponding IR sideband as a function of temperature. Bottom panel: Temperature evolution of the most intense low-frequency Raman bands. The vertical dashed line marks the critical temperature.

this mode is a clear evidence of the influence of the Peierls-mechanism in driving the phase transition. Due to the presence of a few lattice modes with the right symmetry to be coupled with electronic structure, the mode seen in the IR spectrum corresponds to an effective mode, resulting to the superposition of several modes. We cannot follow the frequency evolution down to the transition temperature, since below 80-75 K it becomes impossible to separate the contribution of the two side-bands, letting aside the interference from the fluctuations occurring near the phase transition.

Now we want to search for a possible soft mode in the LT-phase. In this case the Peierls mode(s) should be active in Raman in addition to IR, and we shall investigate them through Raman spectroscopy. Low-frequency Raman also gives indications about the cell doubling, given the difference in the number of phonons present in the LT and HT phases.

Fig. 2.10 shows low-frequency Raman spectra from 10 K up to the transition temperature. The temperature dependence of the Raman frequencies is shown in the bottom panel of Fig. 2.9, both below and above the transition temperature. We notice that the phonons in the HT phase are about a half of those in the LT phase, as expected. One

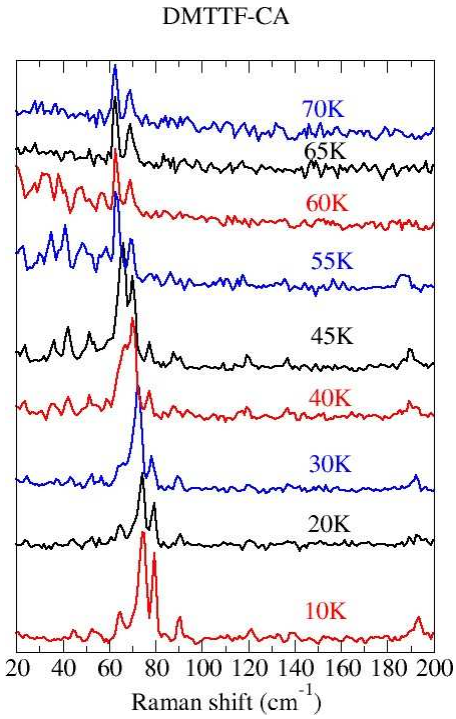

Figure 2.10: Raman spectra of lattice phonons as a function of temperature in the low-temperature phase. Spectra are y-shifted for the sake of clarity.

immediately notice the usual softening for all the modes as we increase the temperature, due to lattice expansion. However, in the LT phase the softening of some phonons is more pronounced close to the critical temperature. The frequency lowering is not as large as in the HT phase (top panel of Fig. 2.9), but is certainly present. The relative weakness of the effect compared to the HT phase can be explained considering that in the HT phase we observe the softening of an "effective" Peierls mode, superposition of several phonons all coupled to the CT electrons. In the LT phase, on the other hand, the softening is distributed on several modes, and the phonon description and mixing changes as we approach the phase transition. The effect is clearly seen in Fig. 2.9, where at about 40 K there is a case of avoided crossing of two phonons located around 70 cm^{-1}. In addition, we have to keep in mind that the DmTTF-CA transition is second order, but cannot be considered a strictly one-dimensional Peierls transition, as the transition implies a change in the number of stacks per unit cell. The actual phase transition mechanism is a complex one, as shown by the fact that just below T_c there is coexistence of two slightly different degrees of ionicity on the molecular sites. This finding might be explained in terms of an inequivalence of the two stacks inside the unit cell in proximity of T_c.

2.6 Discussion and conclusions

The present work does not allow us to draw definitive conclusions about the equivalence or inequivalence of the two DmTTF-CA stacks inside the unit cell of the LT phase (antiferroelectric or ferrielectric arrangement). As just discussed, the presence of two slightly different degrees of ionicity may imply that just after the phase transition we have a temperature interval ($\sim 62 - 54$ K) in which the two stacks are inequivalent with the $P1$ structure [14], followed by a definitive structural rearrangement yielding to the 14 K $P\bar{1}$ structure [11]. This picture would support the $P1$ structural determination [14], collected at 40 K below our coexistence T region, only assuming that the $P1$ structure refers to a non-equilibrium phase. Such "frozening" of a metastable phase may be a consequence of a too fast sample cooling, a case not uncommon in organic solid state, although most of the times refers to some disordered, glassy phase [24].

At this point we wish to underline that inequivalence of the stacks does not necessarily imply an appreciably different degree of ionicity. DFT calculations made for the $P1$ structure at 40 K indeed found practically identical ϱ for the two stacks with different dimerization amplitudes [25]. We may then have a scenario with two (slightly) inequivalent stacks, but practically identical ϱ.

IR spectra polarized parallel to the stack (Fig. 2.4) of course cannot disentangle dimerization amplitudes on different stacks. Optical spectroscopy selection rules, on the other hand, are based on the factor group (unit cell group), therefore reflecting the translational long-range order of the crystal [26]. From this perspective, two findings are in favor of inequivalent stacks, down to at least 20 K. The first fact refers to the Raman-IR coincidence observed for the a_g molecular modes in the LT phase (Fig. 2.8). If the two stacks are equivalent, and connected by an inversion center, each a_g mode of one stack would be coupled in-phase and out-of-phase with the same mode on the other stack. The in-phase mode is Raman active, and the out-of-phase one IR active, therefore we should not observe precise frequency coincidence, the difference being related to the strength of inter-stack interaction. Unfortunately, our data are not conclusive in this respect, due to the frequency uncertainties associated with the Kramers-Kronig transformation.

The other experimental observation that can be explained in terms of inequivalent stacks is the doubling of localized electronic transitions below 65 K [13]. This experimental observation was the first one that induced Aoki *et al.* [13] to suggest the coexistence of neutral and ionic species, but since then it has been almost forgotten. Horiuchi *et al.* [10], as well as the present measurements, exclude such coexistence, and the only explanation we can think of the doubling is in term of ordinary Davydov splitting [26]. However, the two components of the Davydov splitting can be both optically active only in the lack of inversion center relating the two stacks, otherwise the *gerade* component is inactive.

Whereas the above hints favor the ferrielectric structure, we mention that recent NQR experiments seem to imply stack equivalence [16]. We then conclude that the stack

inequivalence in the LT phase, if exists, is certainly very small, and cannot be assessed by spectroscopic measurements. Only the replica of structural measurements and/or of the refinement process starting from the two different hypothesis will definitely settle the question of equivalence-inequivalence of DmTTF-CA stacks. On the other hand, this question is not particularly relevant as far as the mechanism of DmTTF-CA phase transition is concerned. The present analysis departs from the previous ones [10, 11, 12] only in some seemingly marginal details, but actually the resulting picture of the phase transition is completely different.

First of all, we have ascertained that the phase transition implies only a limited change of ϱ, DmTTF-CA remaining well below the 0.5 N-I borderline, on the *neutral* side, as done by other members of the DmTTF-haloquinone series [10, 11]. Therefore the transition can hardly be termed N-I, since cell doubling and stack dimerization clearly constitute the driving force of the transition. Furthermore, our data suggest that the major charge rearrangement follows, by a few degrees K, the onset of cell doubling and stack dimerization. This indication is not definitive, as it has recently been reported that different samples may give slightly different transition temperatures [16]. However, at the light of the present data it is tempting to envision a scenario in which the dimerization and cell doubling lead to a better molecular packing, with an increase in the Madelung energy and consequent small, continuous change in ϱ. The presence of slightly differently charged molecular species before the dimerization/cell doubling has reached completion (Figs. 2.1 and 2.5) fits quite naturally into this picture.

Disentangling the contribution of the cell doubling from that of the stack dimerization is a useless endeavor. In any case, our measurements have clearly evidenced the presence of an effective soft mode along the chain (Fig. 2.9, top panel), so a Peierls-like mechanism is certainly at work in the precursor regime of the phase transition. X-ray diffuse scattering also reveals the importance of electron-phonon coupling along the chain, and of one-dimensional correlations. It has been interpreted in terms of lattice relaxed exciton strings (LR-CT) rather than in terms of a soft mode. The phase transition is then regarded more as a disorder-order transition (ordering of LR-CT exciton strings along and across the chains), and not as a displacive one, with progressive uniform softening of the Peierls mode up to the final chain dimerization. We are currently re-analyzing the X-ray diffuse scattering data to examine whether and to what extent they are compatible with the soft-mode picture. The present results of course only evidence the soft-mode mechanism, and the presence of LR-CT exciton strings cannot be excluded, in particular close to T_c, in the region where our data cannot be unambiguously interpreted.

The LR-CT exciton string picture has been invoked mainly to account for the dielectric constant anomaly at T_c, attributed to the progressive ordering of the a para-electric phase before reaching anti-ferroelectric (or ferrielectric) ordering [11, 15]. On the other hand, it has been shown that the Peierls mechanism is also able to *quantitatively* explain the experimental increase of the dielectric constant at T_c, interpreted as due to charge oscillations induced by the Peierls mode [23].

We underline in this respect that although the dimerization of the stack in the I phase has been often attributed to a spin-Peierls mechanism [9], the electronic degrees of freedom are involved as well, particularly in proximity of the N-I borderline [23]. Furthermore, whereas I stacks are *unconditionally* unstable towards dimerization, N stacks may dimerize, provided the electron-phonon interaction is strong enough [27, 28, 29, 30]. We have shown that this is precisely the present case. Correspondingly, we have an increase of the dielectric constant less important than in the case of TTF-CA [8, 9], as predicted by the calculations [23]. In summary, the present interpretation stresses the importance of the lattice instability over that of charge instability in DmTTF-CA and related compounds.

Chapter 3

Electric field effect on the paraelectric and ferroelectric phases of TTF-CA

3.1 Aim of the work

Neutral-ionic phase transitions occur in a little group of mixed-stack CT organic compounds, and can be induced by temperature and/or pressure, as shortly discussed in Chapter 1. Also the possibility of a transition triggered by electromagnetic radiation have attracted interest [31]. The effect of an external electric field have not been intensively investigated so far. The ferroelectric state exhibited at low temperature from the mixed-stack compound TTF-CA is an attractive target to investigate the ability of an electric field of modifying order parameters like molecular charge or intermolecular distances.

The ferroelectric nature of the low-temperature phase of TTF-CA has been clearly demonstrated. Hysteresis cycles at different temperature were presented by Collet [15]. The system becomes ferroelectric in concomitance with the structural phase transition, and the value of the spontaneous polarization at 78 K, 3 degrees below the transition, is about 0.4 μCb/cm^2. The effect of an alternating electric field in the ferroelectric phase has been investigated by Kishida *et al* [33] by studying the change of the visible reflectivity on a TTF-CA single crystal. Their experiment shows that the electric field is able to modulate the degree of charge transfer, in a direction analogous to a decrease in temperature and can move the domain walls between the two ionic state with different polarization. Another interesting behavior of the TTF-CA ferroelectric phase has been discovered by Tokura *et al* [34]. Measuring the conductivity they observed switching from a low-conductivity state to a high-conductivity state by increasing a static electric field. This transition is reversible and by lowering the field the system comes back to

the low-conductivity phase following an hysteresis loop with an area that increase with decreasing temperature. The phenomenon was also observed in the high-temperature para-electric phase in proximity of the transition temperature while at sufficiently high temperature the change in the conductivity is continuous.

The possibility of modulating the charge transfer with an electric field should also produce modifications in the molecular vibration energy. A spectroscopic study of vibrations in presence of an electric field at various temperatures has not been done up to now, and this has been the motivation of our work.

3.2 Experimental

Electroreflectance measurements have been made in the spectroscopic laboratory of the "Physikalisches Institut 1" of Stuttgart, under the direction of Prof. Martin Dressel. Electric potential has been applied by means of a Keithley 6517A. The crystals used were needles with dimensions of about 0.2-0.4 mm. The highest values of the potential reached (about 300 V) correspond to an electric field as great as 4-8 KV/cm, depending on the crystal size. The field has been applied along the needle axis, coincident with the stack direction. Thermal contact was obtained by gluing the crystal to the sample holder by G.E. paste. Copper wires attached to the crystal with carbon paste have been used for the electric contact. The thermocouple used to measure the heating of the crystal in presence of the electric field was home-made. It consists of Ni/Cr wires attached with G.E. paste to the sample and to the sample holder.

3.3 Results

We have measured the reflectivity in the mid-IR region with an applied electric field at various temperatures, both in the high-temperature and low-temperature phase. By comparing reflectivity with and without the electric field the variation induced by the field can be observed. Static potential was applied along the stack axis and a few hundreds Volt was used with crystals of some tenth of millimeters, corresponds to electric field up to 8 KV/cm of magnitude, as explained above.

Information about the effect of the field on the degree of charge-transfer and structural variations can be obtained. Three different behavior have been found depending from the temperature of the crystal.

In the high temperature region, above the phase transition, in the neutral, "para-electric" phase, the electric field leads the system towards a more neutral phase, i.e. the ionicity decreases and no structural variations are observed. As one can see from the bottom panel of Fig. 3.1, the frequency of the C=O vibration has a blue-shift when the electric field is increased, corresponding to a decreases of ionicity. The top panel of

Fig. 3.1 shows the differential reflectivity, calculated by dividing the spectrum obtained in the presence of the field, by the one without the field. This representation allows one to better evidence the changes induced by the applied field. On the other hand the

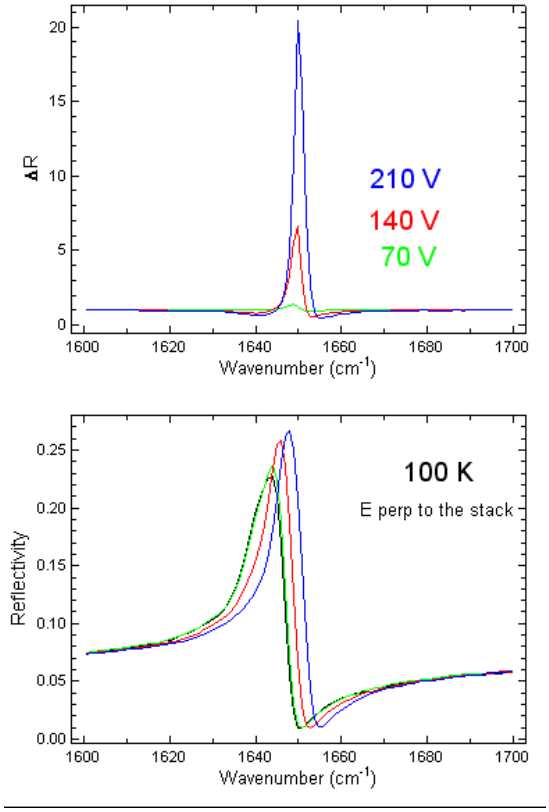

Figure 3.1: Top panel: Differential reflectivity at 100 K at different values of the electric field. Bottom panel: Reflectivity in the C=O stretching region at 100 K for the same values of the electric field.

observation of the reflectivity allows one to directly look at the qualitative behavior of the charge variation.

At very low temperature the effect of the field is little and no phase switching can be observed before the dielectric breakdown which takes place at very high field (Fig. 3.2). Even if differential reflectivity shows some field-dependent effect, the direct look at the absolute reflectivity shows that these effects are not significant and the ionicity does not changes appreciably.

Below the transition temperature, close to the critical temperature, a sufficiently high electric field transforms the ionic-ferroelectric phase in the neutral, para-electric one. In Fig. 3.3 both variations in the polarization perpendicular (left) and parallel

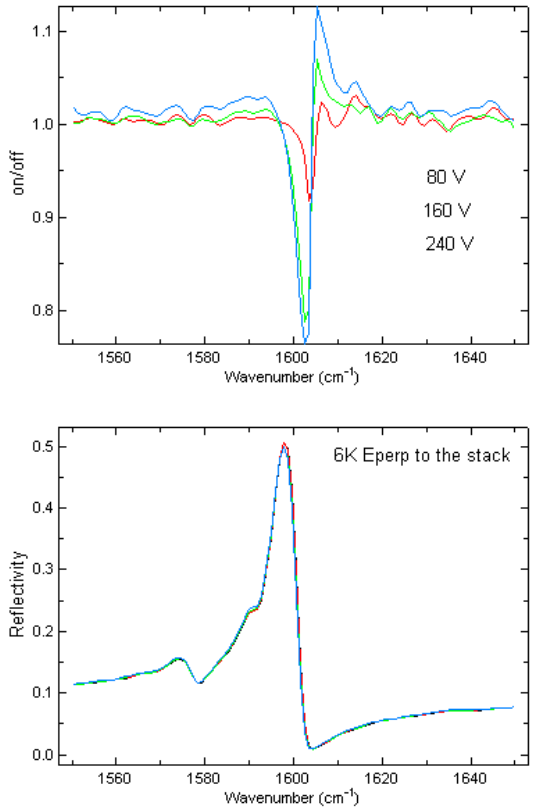

Figure 3.2: Top panel: Differential reflectivity at 6 K at different values of the electric field. Bottom panel: Reflectivity in the C=O stretching region at 6 K for the same values of the electric field.

(right) to the stack axis are reported. The variation of the C=O frequency is high and corresponds to a transformation from the ionic phase to the neutral phase. Differential reflectivity (top of the figure) is characterized from anomalous structures with respect to that observed without a phase transition. Also the disappearance of the vibronic bands, as one can see in the polarization parallel to the stack (right part of the figure), is a signature of the switching from the dimerized stack to the regular one. This electric field induced transition is reversible and when the field is switched-off the system comes back in the low-temperature ionic phase. The critical field necessary to induced a phase switching is temperature-dependent. Fig. 3.5 shows the critical field versus the experimental temperature, down to 30 K. Fields applied below this temperature do not induce the transition, since the high fields required destroy the sample. The behavior seems to be non-linear, suggesting some new mechanism has to be active in the presence of the field. Before measuring the critical field at lower temperature the crystal was

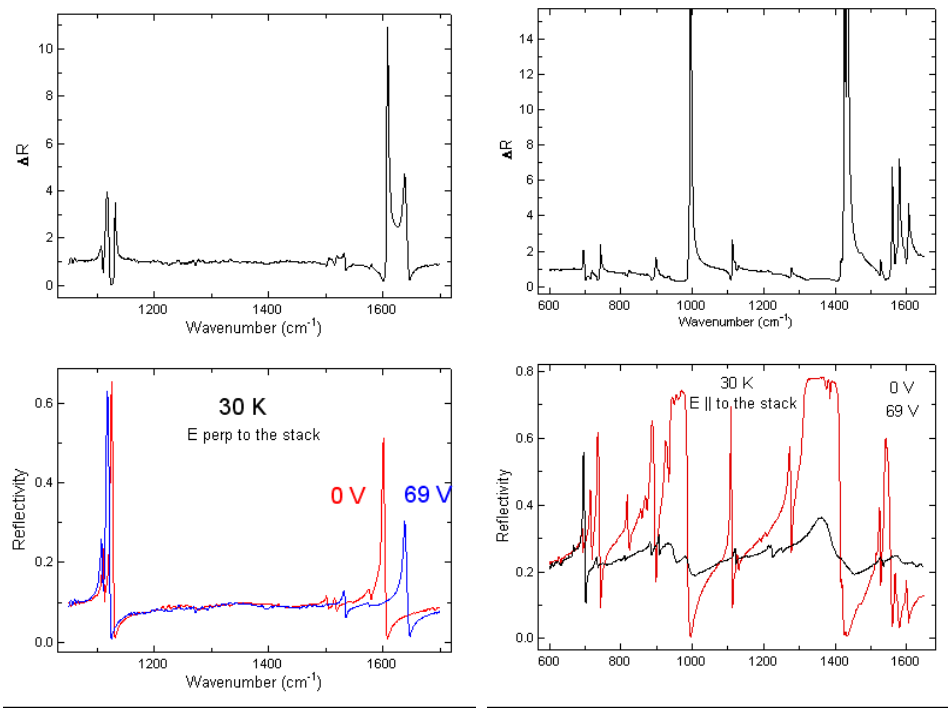

Figure 3.3: Left part: Top panel: Differential reflectivity at 30 K at different values of the electric field. Bottom panel: Reflectivity in the polarization perpendicular to the stack axis at 30 K for the same values of the electric field. Right side: Top panel: Differential reflectivity at 100 K at different values of the electric field. Bottom panel: Reflectivity in the polarization parallel to the stack axis at 100 K for the same values of the electric field.

heated-up above the Curie temperature to eliminate any memory effect. In fact, the critical value depends on the "electrical history" of the sample. For example, when the ionic-neutral switching is induced and the system has came back to the ionic state by lowering the field below a certain value, the critical value to induce the ionic-neutral switching again is not the same as before.

This electric memory effects can be studied by continuously increasing the field with a certain polarity, decreasing it down to zero after the ionic-neutral switching is reached, and repeating the same procedure in the opposite polarity. The results are summarized in Fig. 3.5. Red points show the critical field in the forward direction, i.e. when the field is increased from zero to both high positive and negative values, while the blue ones show the critical field when the potential is lowered from high positive or negative values to zero. The line is a guide to follow the chronological order of the operations, starting from zero field. We immediately note that we can increase the critical field to switch

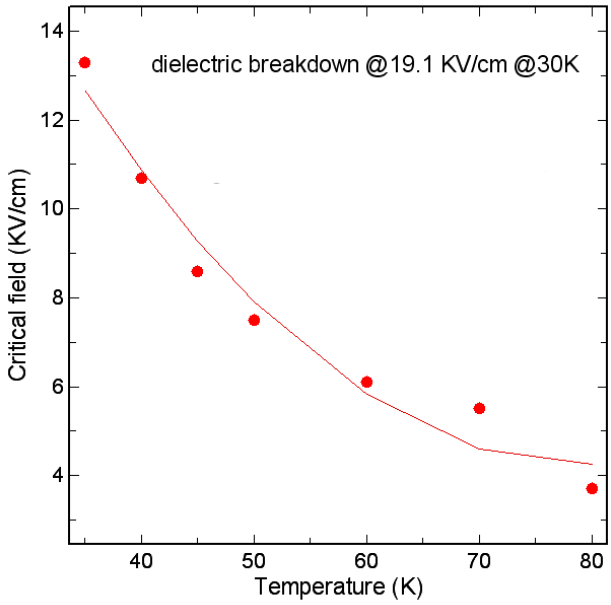

Figure 3.4: Temperature dependence of the critical electric field to switch from the ionic to the neutral phase.

from the ionic-ferroelectric phase to the neutral-paraelectric one, after every potential loop. For example in the first cycle the critical field, in the positive field region, is about 3.5 KV/cm and in the third cycle has reached 5 KV/cm. The blue points (backward cycle) refer to the values to which the electric field has to be reduced to come back in the ionic phase. This value is always lower than that measured in the forward cycle. This implies the presence of a hysteresis region that can be visualized by plotting the ionicity value versus the electric field for a given cycle (Fig. 3.6). The plot puts in evidence the hysteresis region. The graph is divided into two regions by the continuous line. Above it, we are in the ionic phase and below we are in the neutral phase. When a potential cycle begins, in the ionic-ferroelectric phase, the ionicity remains constant at $\rho \sim 0.5$ up to about 3.5 KV/cm, after which the ionicity jump to a value of 0.3. Then if the potential is lowered the ionicity retains its value corresponding to a neutral phase, up about 3 KV/cm, showing a large hysteresis. The potential is then reported to zero and successively inverted. Also in the negative potential region we observe the same kind of behavior. A sort of a memory effect is also observed in this case, because in the negative potential region the hysteresis area differs from that of the positive potential value.

After these first trials, the successive investigations have been focused on the low-temperature ferroelectric phase. The presence of dipolar domains in the crystals and also in the stack, as schematically represented in Fig. 3.7, make possible a series of

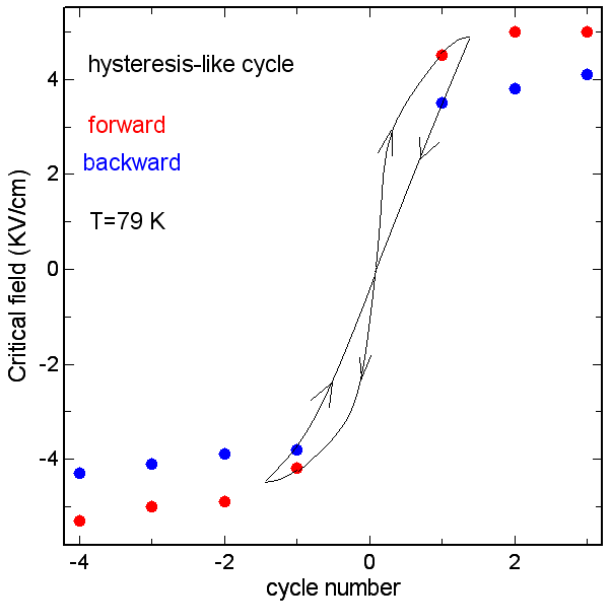

Figure 3.5: The dependence of the critical electric field to induce the switch from the ionic to the neutral phase, from the number of phase switching cycles. Red points indicate the critical field for the ionic-to-neutral switching. Blue points indicate the value to decrease the electric field to come-back in the ionic phase.

peculiar experiments using an electric field. We know that in a ferroelectric an electric field enlarge the domains that are oriented in the same sense as the external field at the expense of the opposite domains. Microscopically this coincides with the breaking of pair of molecules dimerized in the sense opposite to the external field and probably to a variation of charge-transfer inside the dimers. Now we want establish in what measure these effects influence the molecular vibrations or whether we are measuring other consequences that are not typical of ferroelectrics. The first question we address is the dependence of the differential reflectivity from the direction of the external field. The d.c. field is invariably applied along the stack axis, but the polarity can be reversed. Fig. 3.8 shows the differential reflectivity in the C=O stretching region at different values of the external field, and at different polarities (plus: top panel; minus: bottom panel), at a fixed temperature. The differential reflectivity has no sign-dependent shape meaning that the variations in the reflectivity spectra are qualitatively the same. To avoid any memory effects these two experiments were done in two different cooling-cycles, each time starting from the high-temperature phase and cooling down to the reported temperature value without any external field.

The same kind of experiment was performed after the crystal was cooled in the

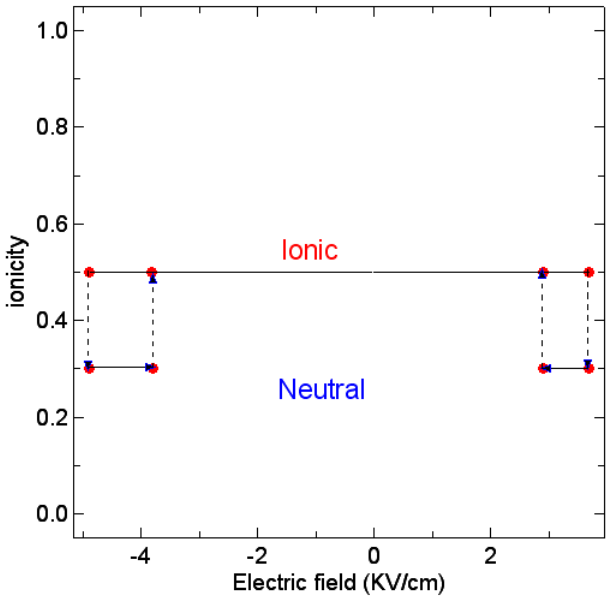

Figure 3.6: Hysteresis region during ionic-neutral transformation. The area differ for positive and negative field values.

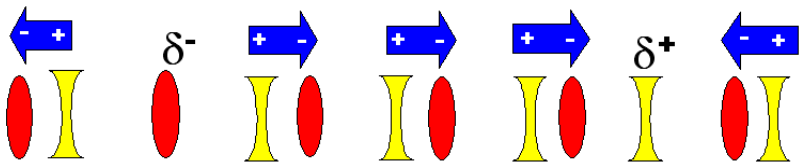

Figure 3.7: Schematic picture of the ionic-dimerized stack. The formation of domains with different polarization is put in evidence.

presence of an external electric field. In this way macroscopic domains with polarization parallel to the external field may be favored with respect to the anti-parallel ones, and at low temperature the area of these domains should be greater than that of other kind of domains. Also in this case no sign inversion in the band shape was detected, demonstrating one more time the insensitivity of the intra-molecular vibrations to the direction of the internal macroscopic polarization.

We have also performed an hysteresis-like loop. The electric field is increased up to a certain value, less than the critical one, to avoid any effect of a change of state, and then is decreased down to zero and then reversed and increased again in this new direction and so on. One can observe that the band shape depends quantitatively from the value of the

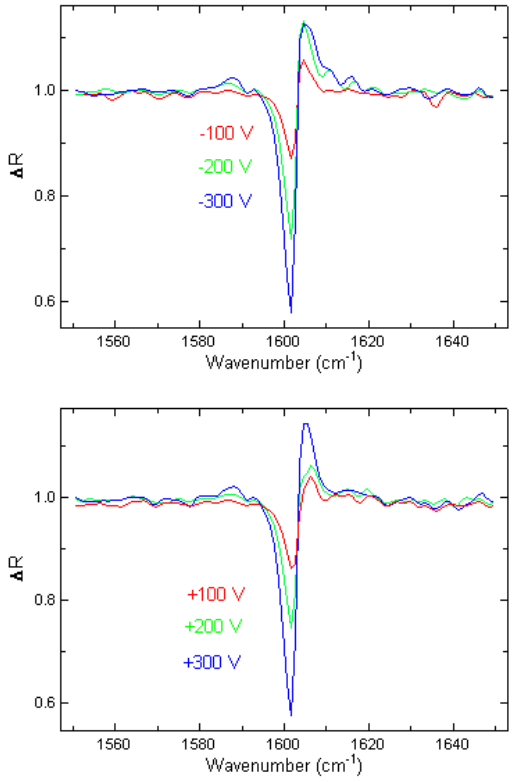

Figure 3.8: Differential reflectivity, in the ionic phase, for several values of the electric field.

field. From Fig. 3.9 one notes that when the field is increased, the reflectivity variations become more pronounced and decrease when the field is decreased, without disappearing when the potential reaches zero. This behavior looks like a remnant polarization effect. When the polarity of the field is reversed the differential reflectivity does not change the shape, showing no sign inversion. So in general we have to conclude that vibrational modes are not sensitive to the inversion of the resultant polarization of the overall crystal obtained by reversing the electric field. From the figure is also evident a certain type of "memory effect". In fact, for example, the changes at zero field are not absent when the field is lowered from its maximum value and the absolute value depends of the electric history of the crystal as one can observe from the same value of the field with different sign.

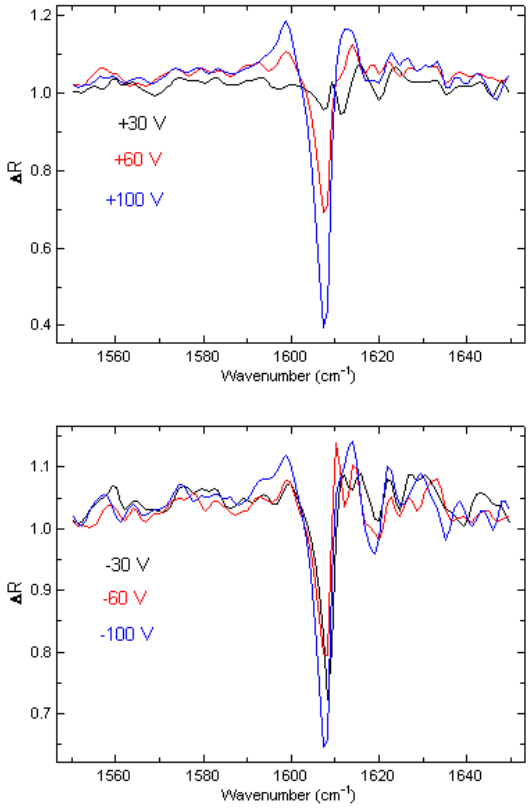

Figure 3.9: Differential reflectivity, in the ionic phase after the field-cooling process, for several values of the electric field.

3.4 Discussion and perspectives

TTF-CA differs from a classical ferroelectric because in the ferroelectric phase a field sufficiently high can destabilize the ferroelectric phase with respect to the paraelectric one. So, in a hysteresis-like cycle when a critical field value is exceeded, a switch between these two phases is obtained. This means that the ferroelectric phase is destroyed, differently from any other classical ferroelectric compound.

Up to now we did not consider the possibility that the observed effects are attributable to a temperature increase. Apart from the very complicated behavior of the hysteresis and of memory effect, the trend in the ionicity, when the static electric field is applied, is in the same direction of that produced by a thermal effect. Then it is important to determine how great the temperature variation is, and eventually discriminate between the effect of the electric field and the effect of the temperature. We have to keep in mind that an electric field produces a current, the value of which depends on

the insulation properties of the examined crystal.

Two experiments have been done to have some insight about the temperature increase. The first has been a direct measure of the current running through the crystal, so that by means of the Joule law, an estimation of the power dissipated by the crystal can be achieved. High power could give rise to a non negligible thermal effect and add itself to the electric field effect. Unfortunately, the performed current measurements cannot be considered sufficiently reliable, and in any case the power dissipated does not give an indication of the temperature increase in the lack of information about the power dissipation of the sample. The second experiment has been to directly measure the temperature of the crystal, with the aid of a thermocouple. A few attempts have been done, by building and putting a thermal sensor onto the crystal. Our apparatus worked by measuring the temperature difference between the crystal and the cold part of the cryostat. The crystal was glued to a sapphire plate with G.E. glue, and sapphire was put onto the cold-finger with carbon paint.

The electric field was applied for a time of 40 seconds and then switched off. This procedure was repeated many times, with an increasing field each time, and the temperature difference increases between the crystal and cryostat monitored continuously. Fig. 3.10 shows the results in the low-temperature ionic phase at 60 K. The field gener-

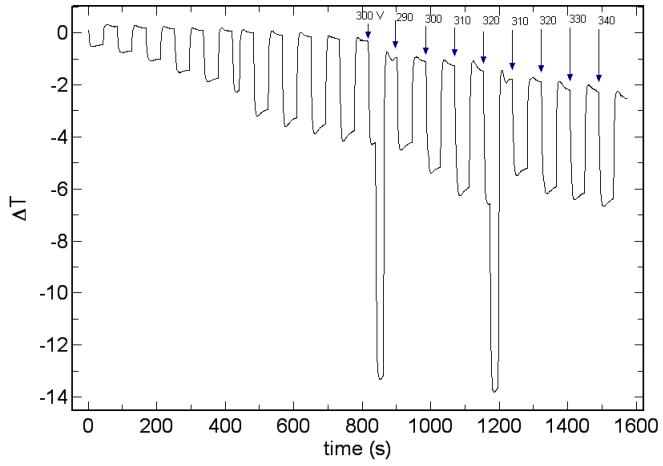

Figure 3.10: Temperature variation induced by the electric field at 60 K. The value of the potential are indicated in the top of the figure.

ates a significant temperature increase, that however is not sufficient to go in the high temperature phase above 81 K. The heating increases as the field is increased, and when the potential is sufficiently high, 300 V in this run, one can see the effect of ionic-neutral switching. The large temperature variation observed (14 degrees), is due to the phase

transition and cannot be interpreted like a real heating effect because the high temperature phase has physical properties, like thermal capacity and thermal conductivity, completely different from the low temperature phase. The numbers indicated in the top of the figure are the values of the applied voltage. Also in this measurements it is evident the memory effect discussed above, and one can see that after the ionic-neutral switching has been induced by the field, the next cycle needs a more high voltage to obtain the same transition.

The same experiment has been repeated in the high temperature phase. Also in this

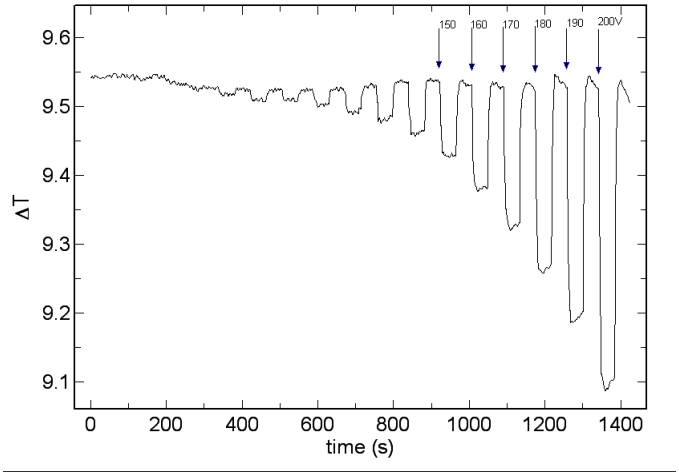

Figure 3.11: Temperature variation induced by the electric field in the higt temperature phase. The value of the potential are indicated in the top of the figure.

phase we observe the same behavior as before but the temperature variations are very little (Fig. 3.11).

In conclusion, our preliminary spectroscopic study on the organic ferroelectric TTF-CA mixed-stack compound shows many intriguing phenomena related to the particular nature of the phase transition in a typical 1D organic charge-transfer system. After these measurements we can conclude that, although some typical behavior of a ferroelectric can be discerned from it, other characteristic phenomena are lacking, demonstrating that, although the intra-molecular vibrations are very sensitive to the electronic and structural variation, they cannot clarify all the aspects presented here. The main result of the experiments up to now is the possibility to transform a ferroelectric state in a paraelectric one. This is not common in the field of ferroelectricity, where an electric field creates a "more ferroelectric" state, without destroy the ferroelectric order. So there are two possibilities:

1. The organic ferroelectric TTF-CA differs from typical ferroelectrics due to the

particular phase transition it is subject. Also the relationship between ionic and neutral phases and ferro- and para-electric phases could be not clear at all.

2. The effects we observe are predominantly due to an heating effect and not directly to the electric field.

We have to add that non-precise temperature control did not allow us to evaluate how much this temperature increase is important in determining the measured effects. Both types of experiments have to be replicated. A way to minimize the temperature effects could be to perform the experiment in nitrogen atmosphere, in order to improve the heat dissipation on the crystal surface. To rule out a temperature increase, more accurate measurements are needed, and also a better control of the temperature is necessary, in particular, the elimination of the thermal hysteresis is essential to interpret in the proper way all the observed phenomena.

Part II

One-component organic molecular materials

Chapter 4

Organic semiconductors

4.1 Polymorphism and phase purity

Over the past decade, π-conjugated oligomers such as the oligoacenes, oligophenylenes and oligothiophenes have been widely studied for developing a new generation of organic-based devices. Their properties are suitable for use in transistors, light emitting diodes, lasers and non-linear optic devices[35, 36, 37]. Organic semiconductors have many advantages over their inorganic counterparts. They offer the possibility to be solution-processed allowing the fabrication of devices such as circuits, displays on plastic substrate (Fig. 4.1). They can also deposited by unconventional methods, such as inkjet and screen printing.

The most attractive perspective, however, is the incorporation of new functionalities by chemical modifications. The versatility of organic synthetic techniques and the wide spectrum of commercially available building blocks allow seemingly infinite flexibility in tuning molecular packing and macroscopic properties. The opportunity to design application-specific materials could offer not only vast improvements in current devices, but also enable several new applications. Applications currently reaching the commercialization stage involve for instance the use of organic π-conjugated polymers[38, 39] and molecules[40, 41] as active elements in light emitting diodes (LEDs). The integration of polymers into nanoscale heterostructures is offering great hope for high-efficiency, low-price organic solar cells (Fig. 4.2). Organic semiconductors such as pentacene and rubrene have surpassed amorphous Si in performance, and their use as the semiconducting layer in field-effect transistors (FETs) represent another pole of high technological relevance. Although thin film or polymers form are the most suitable for the practical use of such materials, the optimization of the device performances stimulates the research towards understanding intrinsic properties, a goal that can be achieved through the study of single crystals. The problem affecting the transport properties or the emission efficiency are under active investigations. Two important problems one has to

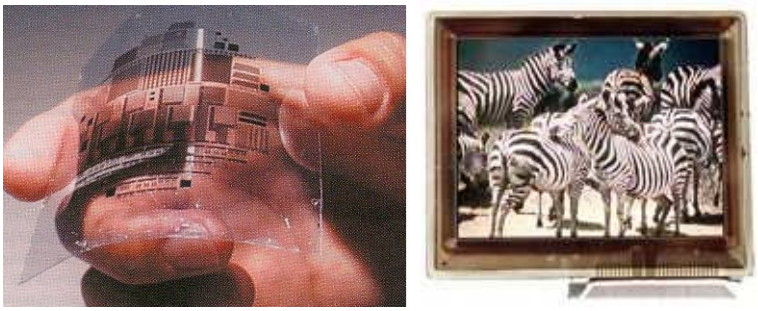

Figure 4.1: Field-effect transistors into a plastic substrate (left) and display (right) made up of organic LEDs.

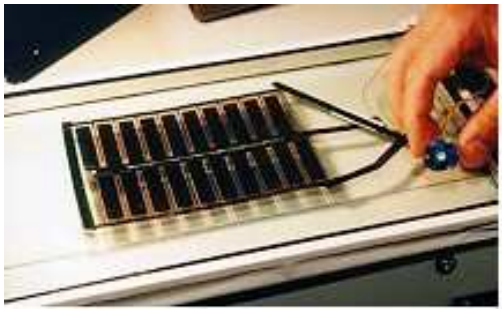

Figure 4.2: Organic solar cells.

overcome are the chemical purity of the sample, improved by purification techniques, and the polymorphism in the crystalline arrangement. This last aspect is typical of organic molecular materials, since the forces keeping together organic molecules are weak and mostly non-directional.

Spectroscopic investigations in the region of lattice phonons have been shown to be a powerful technique in the identification of phase purity [66]. It is a easy, non-destructive and fast experimental tool for in-situ characterization. Furthermore the investigation of the vibrational structure of organic semiconductors gives us some insight about the role of phonons in the absorption and luminescence optical processes and in their electric transport properties . In this second part of the thesis we address the study of lattice phonons to identify the lattice phonons and the possible presence of different polymorphs in two organic semiconductors, α-quaterthiophene and rubrene.

4.2 Computational and spectroscopic methods

The crystal structures and the vibrational frequencies of α-quaterthiophene and rubrene have been calculated following a well assessed treatment, combining *ab-initio* methods for the isolated molecule and empirical atom-atom potentials for the crystal[53, 54].

Equilibrium geometry, atomic charges, and vibrational modes of the isolated molecules are computed by the Gaussian03 program[55], with the B3LYP density functional and the 6-31G(d) basis set. The atomic charges are fitted to the *ab initio* electrostatic potential (ESP)[55]. The crystal is initially described in terms of rigid molecules (Rigid Molecule Approximation, RMA). The crystal total potential energy, Φ, is given in terms of an atom-atom Lennard-Jones model, with the parameters of the AMBER force field[56], combined with an electrostatic contribution described by atomic charges q_i, q_j:

$$\Phi = \frac{1}{2}\Sigma_{i,j}[q_i q_j / r_{i,j} + A_{i,j} exp(-B_{i,j} r_{i,j}) - C_{i,j}/r_{i,j}] \tag{4.1}$$

where $A_{i,j}$,$B_{i,j}$ and $C_{i,j}$ are empirical parameters for each type of atoms. For large molecules such as α-quaterthiophene and rubrene it is necessary to go beyond the RMA. The coupling between molecular and lattice vibrations is introduced through the exciton-like method[53, 54], using the *ab-initio* vibrational Cartesian displacements and frequencies of isolated molecule.

The effects of temperature are accounted for by computing the structures of minimum Gibbs energy, $G(P,T)$, with a Quasi Harmonic Lattice Dynamics (QHLD) method[53]. In this method, where the vibrational Gibbs energy of the phonons is estimated in the harmonic approximation, the Gibbs energy of the system is

$$G(P,T) = \Phi + pV + \Sigma_i h\nu_i/2 + k_B T \Sigma_i ln[1 - exp(-h\nu_i/k_B T)] \tag{4.2}$$

where V is the molar volume, $\Sigma_i h\nu_i/2$ is the zero-point energy and the last term is the entropic contribution. The sums are extended to all phonons frequencies ν_i.

As mentioned in the previous Chapter, it is now well established that Raman spectroscopy is a valuable tool for non invasive, *in-situ* recognition of polymorphs [66]. Here, we shortly summarize the method, as it concerns a rather new methodology in Raman spectroscopy . When polymorphism occurs in molecular crystals, the chemical identity in the different crystal phases implies very similar or identical spectra for the intramolecular vibrational modes of different polymorphs. One should then focus the attention on inter-molecular modes, i.e., collective translational or rotational motions of the molecules in the unit cell. These modes produce dynamical deformations of the crystal lattice called lattice vibrations or lattice phonons, whose frequencies, involving Raman shifts in the range 10-150 cm^{-1}, probe the intermolecular interactions and hence are very sensitive to different molecular packing. Because each crystal structure has its own

dynamics, in organic molecular crystals lattice phonons are the fingerprints of the individual crystal structure. Typical examples of the application of Raman spectroscopy to polymorphism in organics are pentacene [42, 43], tetracene [45] and α-sexithiophene [44]. Fig. 4.3 shows the identification of the two polymorphs of pentacene and α-sexithiophene by means of their lattice phonons spectra.

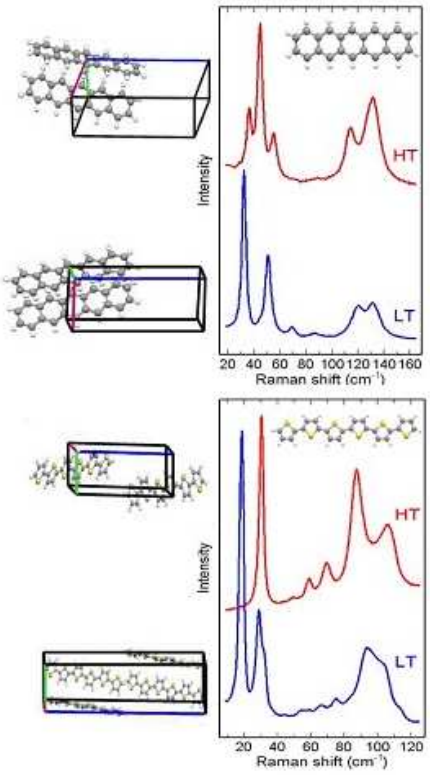

Figure 4.3: Lattice phonons Raman spectra of the two polymorphic form of pentacene and α-sexithiophene and their corresponding crystal structures.

The physical purity (phase homogeneity) of a crystal is directly related to crystal phase identification. Different crystal phases can coexist as different domains in the same crystallite, originating a phase mixing which ultimately affects the physical purity of the sample [65]. The use of an optical microscope coupled to the Raman spectrometer and making the microscope confocal allows the scaling down in size of the crystal region under investigation. Raman scattering is transmitted to the spectrometer only from the restricted sampling volume determined by the focused region of the laser beam, enabling fine tuning of XYZ discrimination. Spatial resolution down to 1 μm and less can be easily achieved. The problem of phase mixing is well known in thin films [46, 47], and is one

of the reasons of the difficulties in obtaining reliable structural characterization. This problem is relevant also for single crystals and a typical example is shown in Fig. 4.4. Once the spectral profiles of the single polymorphs are identified by lattice phonon Raman spectroscopy, they are used as reference spectra and it is easy to monitor physical impurities in which domains of one polymorph embedded inside the other. As reported

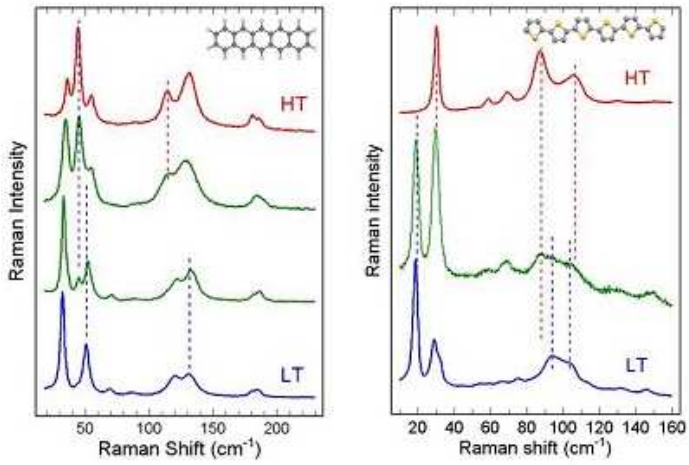

Figure 4.4: Examples of phase mixing in crystalline pentacene and α-sexithiophene.

in Fig. 4.4 for crystalline samples of pentacene and α-sexithiophene, the coexistence of phases appears as an overlap of distinctive phonon bands of either polymorph in the same crystal grain (green traces), as indicated by the vertical bars with reference to the pure polymorph spectra. Phase mixing, or physical inhomogeneities, is observed in most cases where polymorphism occurs [42, 44], demonstrating the general validity and the sensitivity of this technique for detecting the presence of domains of either structure at the μm scale.

It is of great importance to find a suitable method for checking phase homogeneity in each crystal domain by obtaining a visual display of the physical purity. This task can be nicely fulfilled by confocal Raman mapping (CRM) in the region of lattice phonons (10-150 cm^{-1}), outlining a further application of confocality to micro-spectrometry techniques. By scanning the surface, typically few tens of mm wide, with steps as close as 1 μm, one can obtain a series of Raman spectra which can be collected, point by point, in an actual map to be compared to the optical image of the original sample [65, 48], as schematically shown in Fig. 4.5. This will yield crucial information on the topography of each crystal whose phase homogeneity needs to be checked. The spatial resolution is given by the laser spot area and is ranging from 0.88 to 1.05 μm, depending on the numerical aperture of the microscope objective and on the wavelength of the laser line.

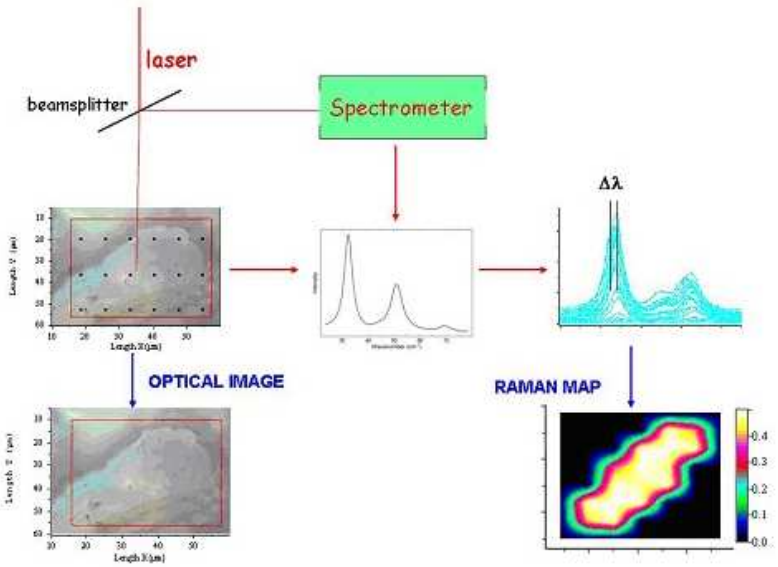

Figure 4.5: Scheme of a confocal Raman mapping experiment.

The actual recipe of the lattice phonon CRM technique can be summarized in four steps:
1. Assign spectra to structures;
2. Scan selected crystal regions;
3. Identify phase mixing;
4. Map structural homogeneity.

The first step requires a careful micro-Raman investigation of a large number of crystalline samples grown in as many conditions as possible, to search for all possible polymorphs. This will yield a series of "reference spectra", each corresponding to a distinct polymorph. This also enables one to select suitable wavenumber windows typical of each crystal phase. The second step concerns the choice of the specimen regions to be investigated, planning a number of point spectra sufficient to reconstruct spectroscopically the sample with a good spatial resolution. In the following step the identification of phase mixing is achieved by comparing complex spectral profiles with the reference spectra of the pure polymorphs. The final step eventually yields the phase Raman mapping of the selected crystal domain, which is obtained by monitoring the spectral windows where either one or the other polymorph shows phonon bands. The relative amount of one phase with respect to the other can therefore be quantitatively represented by the intensity ratio of selected bands and at once converted, with a suitable software, in a conventional palette of colours. For instance, when both A and B forms are present, one can represent the intensity ratio A/B by adopting a blue-green color for the A

phase, while the red-yellow shades correspond to an increasing amount of B phase. A deconvolution of the phonon bands with background suppression will assure a reliable representation of the data. The spread of colors indicates the extent of the phase mixing between the two polymorphs analyzed in the chosen crystal domain. Phase purity obviously is obtained when the overall color remains virtually homogeneous throughout the whole surface scanned. Phase mixing is instead represented by a different extent of one phase inside the other and produces marked differences in the color conventionally chosen as reference of either polymorph. Examples of lattice phonon CRM are given

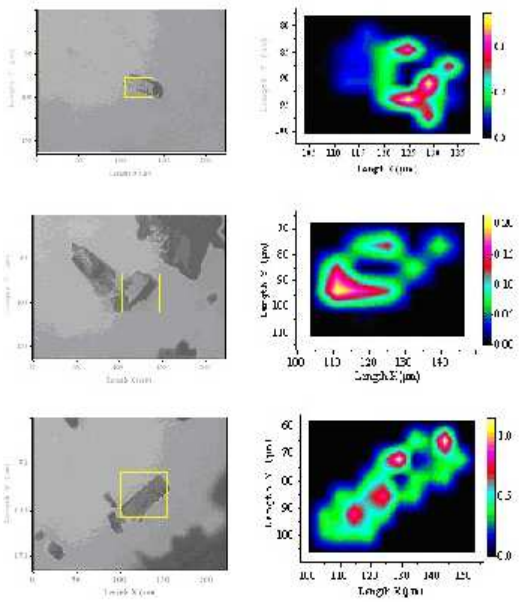

Figure 4.6: Optical (left) and Raman (right) images of selected pentacene crystals. Raman mapping refers to the area XY (μm^2) drawn as a box over the optical image of the crystal. In the Raman maps the color drifts from blue (full H phase) to green/red (increasing amount of C phase). The color scale is selected each time to emphasize the phase mixing in the crystal grain (from [65]).

in Fig. 4.6 and Fig. 4.7 for pentacene and α-sexithiophene, respectively. A variety of situations is observed in pentacene which shows a different extent of phase mixing in three selected crystals whose optical images are otherwise homogeneous. Pentacene was the very first example of an organic material mapped with this technique [65]. In the case of α-sexithiophene the sample in the lowest part of the Fig. 4.7 is a nice example of phase purity, showing a full homogeneous colour, in spite of a large expansion of the conventional color scale. Phase mixing is instead represented by a different extent of one phase inside the other and produces differences in the colour maps, as shown for

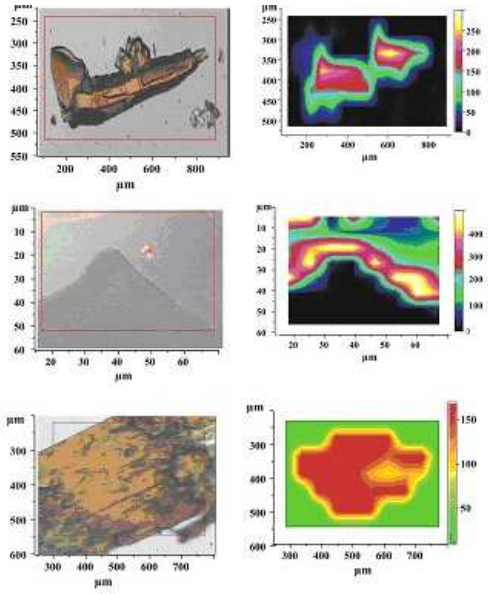

Figure 4.7: Optical images (left) and Raman maps (right) of α-sexithiophene crystalline samples exhibiting phase inhomogeneity. Raman mapping refers to the area XY (μm^2) drawn as a box over the optical picture of the crystal. In the Raman maps the colour drifts from blue-green (LT phase) to red-yellow (increasing amount of HT phase). The colour scale is selected each time to emphasize the phase mixing in each crystal grain (from [48]).

the other two specimens (top and middle sets of Fig. 4.7). As expected, the contours of the optical images are nicely reproduced in the corresponding Raman maps, yielding direct information on which crystal phase is present and in what extent. Furthermore, the comparison between the optical images and the Raman maps show with clear evidence that no relationship exists between morphology and crystal phase: structural information and phase mixing can be efficiently monitored only by Raman maps. It is then crucial to perform a spectroscopic test in order to verify the phase purity in all crystals treated, especially for those cases in which crystal morphology cannot assist phase recognition. It is thus conclusively shown that lattice phonon CRM is a most efficient tool to identify polymorphs and their mixing in the same crystallite at a μm scale. An additional feature related to the confocality of the micro-Raman technique concerns with the possibility to probe phase homogeneity of crystal domains at different sample depths [65, 48]. This is illustrated in Fig. 4.8, where lattice phonon Raman spectra, taken on the very same spot in a given crystal domain, show a variation of the relative amount of either polymorph on penetrating inside the bulk. This is achieved by probing the sample surface at different penetration depths by focusing the laser light

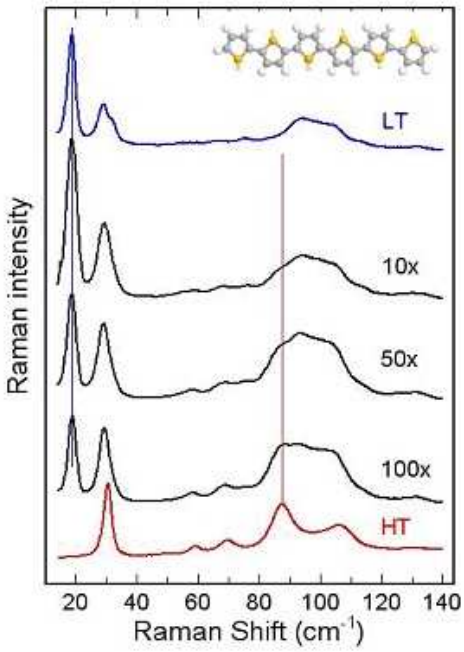

Figure 4.8: An example of Raman phonon spectra of α-sexithiophene taken with different microscope objectives, as labeled. The penetration depth increases from the bottom to the top spectra (in black) of the figure. For better reference, HT and LT lattice phonon spectra are also reported.

with microscope objectives having different numerical apertures. Typical values of the theoretical penetration depths vary from 7.5 μm (100x) to 25 μm (50x) up to a depth of about 450 μm (10x). On getting into the bulk, different amount of phase mixing is found, with an increase of the fraction of LT polymorph, as indicated by the vertical lines that monitor both phases with their reference phonon. It is then important to remark that phase inhomogeneity is not confined to the first layers of the crystal surface, but it propagates into the bulk. The possibility of a three dimensional investigation of single crystal homogeneity is thus an additional appealing feature of this technique applied to heterogeneous solid phases.

Chapter 5

Lattice phonons Raman spectroscopy of α-Quaterthiophene

5.1 Crystal structure of α-Quaterthiophene

α-quaterthiophene (4T), grown by physical vapor phase transport technique [49], crystallizes in two different structures depending on the crystal growth conditions. Depending on the temperature on the source, two polymorphs can be obtained, namely the low-temperature (LT) and high-temperature (HT) phase. LT phase grows at a source temperature of 140 °C in the form of platelets with size up to 1 mm diameter and 1 μm thickness. At a source temperature of 160, 180 or 200 °C platelets of the HT phase, with a diameter up to 2.5 mm and thickness in the micrometer range are formed. At higher temperatures the source material partially melts [50]. The X-ray structure of 4T single crystals has been solved simultaneously by two groups [50, 51]. The two structures differ by the number of molecules in the unit cell ($Z = 4$ or $Z = 2$). They present the herringbone packing common to all unsubstituted oligothiophenes. The molecules are practically planar, the central ring being exactly parallel, and outer ring being twisted by only 1° with respect to the inner ones [51]. In both polymorphs each molecules is surrounded by eight other molecules: four contacts at the end and four contacts laterally.

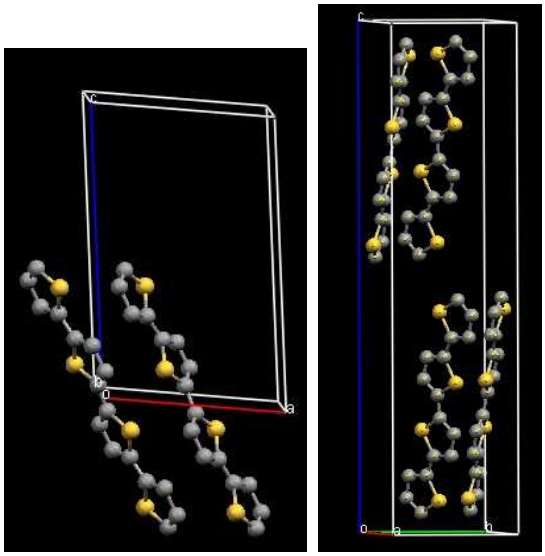

Figure 5.1: Quaterthiophene: HT ($P2_1/a$) and LT ($P2_1/c$) crystal structures.

Table 5.1: Crystallographic information of the two polymorphs of 4T.

data	α-4T/LT	α-4T/HT
Space group	$P2_1/c$(Nr.14)	$P2_1/a$(Nr.14)
a[Å]	6.085(2)	8.935(2)
b[Å]	7.858(2)	5.751(1)
c[Å]	30.483(8)	14.340(3)
β[°]	91.81(2)	97.22(1)
Volume[Å^3]	1456.8(7)	731.0(3)
Z	4	2
Calculated density[g/cm^3]	1.511	1.511

5.2 Spectral prediction in the rigid molecule approximation (RMA)

To predict the number of intermolecular vibrational modes of 4T we adopt for the two polymorphs the space group symmetry $P2_1/c$ for the LT phase and $P2_1/a$ for the HT phase. With this choice c is the longest axis for both polymorphs. A schematic view of the unit cell for the two polimorphs with the indication of the crystallographic axes is reported in Fig. 5.2. In this context, it is important to note that in the HT structure

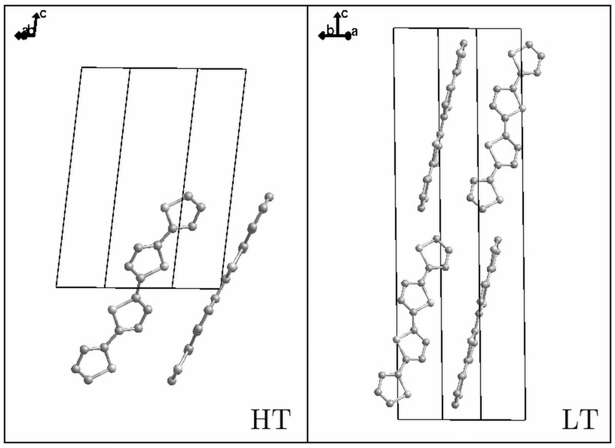

Figure 5.2: Quaterthiophene: HT ($P2_1/a$) and LT ($P2_1/c$) crystal structures.

the 4T molecules lie on inversion centers, whereas in the LT phase they are in general position. This fact has important consequences on the optical $\mathbf{k} = 0$ selection rules, that in the RMA can be easily obtained by the correlation method [52]. This method is based on the relationship between the symmetries of the isolated molecule in the gas phase, of the molecule inside the crystal (site group), and the symmetry of the crystal (factor group). The site group is a subgroup of both the molecular and the factor group. Therefore it establishes a link between the symmetry species of the two groups, as shown by the curl brackets in Table 5.2 for both the 4T structures. We assume the ideal C_{2h} symmetry for the isolated molecule, with the z axis coincident with the binary axis (normal to the molecular plane), and the x axis coincident with the long molecular axis. Thus the molecular rotations R_x, R_y and R_z belong to the *gerade* species, and the translations T_x, T_y and T_z to the *ungerade* ones, as indicated in the left column of Table 5.2. Since in the HT phase the molecules reside on inversion center, the separation between *gerade* and *ungerade* modes is maintained, and in the crystal there are 6 Raman active phonons, $3A_g + 3B_g$, corresponding to in-phase and out-of-phase combinations of the molecular librations of the two molecules in the unit cell. In the LT phase, on the other hand, molecular librations and translations mix through the C_1 site symmetry, so in the crystal we expect 12 Raman bands, $6A_g + 6B_g$. Both the $6A_g$ and the $6B_g$ modes will be described by a mixture of molecular librations and translations. For the sake of completeness, in the rightmost column of Table 5.2 we report (in parenthesis) the components of the crystal polarizability tensor, i.e., the Raman polarization directions. Thus A_g modes are active in the $(aa), (bb), (cc)$, and (ac) polarizations, the B_g ones in the (ab) and (bc) ones.

Table 5.2: Correlation diagram for the two phases of 4T.

Phase	Molecule	Site	Cell
4T/HT	C_{2h}	C_i	C_{2h}^5 $(P2_1/a)$
	$a_g[R_z]$	A_g	$A_g(aa, bb, cc, ac)$
	$b_g[R_x, R_y]$		$B_g(ab, bc)$
	$a_u[T_z]$	A_u	$A_u(b)$
	$b_u[T_x,\ T_y]$		$B_u(a, c)$
4T/LT	C_{2h}	C_1	C_{2h}^5 $(P2_1/c)$
	$a_g[R_z]$	A	$A_g(aa, bb, cc, ac)$
	$b_g[R_x, R_y]$		$B_g(ab, bc)$
	$a_u[T_z]$		$A_u(b)$
	$b_u[T_x, T_y]$		$B_u(a, c)$

5.3 QHLD calculations

To compute eigenvectors and vibrational frequencies of the α-quaterthiophene we have followed the procedure reported in Sec. 4.2. We first computed *ab initio* molecular geometry, atomic charge, vibrational frequencies and Cartesian eigenvectors of the normal modes for the isolated 4T molecule. Constraining the 4T molecule to be centrosymmetric yielded an imaginary vibrational frequency for an out-of-plane molecular torsion of a_u symmetry. Thus, the C_i molecular symmetry does not correspond to an energy minimum, but rather to a saddle point. By deforming the molecule along the mode with imaginary frequencies, we obtained a stable minimum with C_1 symmetry. We have taken the frequencies computed in C_1 symmetry, with the standard scaling by 0.9613 recommended for the combination B3LYP/6-31G(d) [57], and associated them to the eigenvectors calculated in C_i symmetry. Only modes below 340 cm^{-1} were included in the calculations, since higher frequency intramolecular modes do not couple significantly with the lattice phonons.

The crystal was initially described in terms of rigid molecule (RMA), with the *ab initio* C_i geometry. The computation of 4T lattice phonons within the RMA obviously reflect the above symmetry-based predictions. In Table 5.3 we report the QHLD frequencies computed at 300 K for both 4T/HT and 4T/LT. We also report the percentage of librational (%R) and translational (%T) character derived from the analysis of the eigenvectors. Whereas for 4T/LT only the Raman active *gerade* phonons are shown, for 4T/HT we report also the infrared active *ungerade* phonons (both acoustic and optical), to illustrate the connection that may occur between the phonons in the two phases, as the HT unit cell contains one layer of 4T molecules, and the LT one contains two layers (Fig. 5.2). For instance, a look at the phonon eigenvectors shows

that the lowest frequency A_g mode of the LT phase, computed at 6 cm^{-1}, and having 100% translational character, corresponds to the B_u acoustic mode of 4T/HT shown in Fig. 5.3. Analogously, the 4T/LT A_g phonon computed at 97.2 cm^{-1} corresponds to

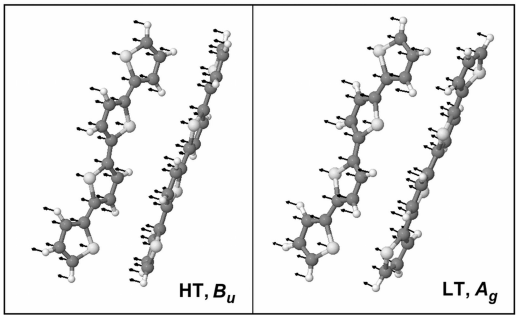

Figure 5.3: Pictorial representation of 4T eigenvectors for one of the two 4T/HT B_u acoustic phonons and for 4T/LT A_g lowest frequency phonon computed at 6.0 cm^{-1}. For the sake of clarity, only 2 of the 4 molecules per unit cell of the 4T/LT phase are shown.

the B_g 4T/HT phonon at 102.0 cm^{-1}. Other examples can be found, but actually the above correspondence cannot be extended to all the modes, since we are not dealing with a true cell doubling. Moreover, direct comparison is prevented when mixing of translational and rotational motions occurs in the 4T/LT phase.

5.4 Lattice phonons Raman spectra and spectral assignment

The assignment of the Raman lattice phonon bands of both 4T polymorphs is made on the basis of room temperature polarized spectra collected from the most commonly developed crystal face, *ab* [58, 59]. We also have recorded unpolarized Raman spectra of polycrystalline samples, at 300 and 10 K. The single crystal polarized spectra allow unambiguous symmetry identification of the modes, whereas some bands which are either weak or overlapped to other bands in the *ab* plane spectra can be identified and disentangled in the spectra of thicker polycrystalline samples at different temperatures. Furthermore, QHLD calculations offer a guide in the spectral interpretation.

In the polarized spectra, the crystal axes are identified by observation under a polarizing microscope [59], and the Raman spectra are then recorded with the polarizations (*aa*), (*bb*) and (*ba*), where the two letters in parenthesis indicate the polarization direction of the incident and of the scattered radiation, respectively [52]. According to the Raman selection rules of Table 5.2, the A_g phonons are active in the parallel polarizations (*aa*) and (*bb*), and the B_g ones in the crossed polarization (*ba*). Of course, both A_g

Table 5.3: Lattice phonons frequencies (cm^{-1}) of 4T/HT and 4T/LT, calculated within the rigid molecule approximation (RMA).

4T/HT	$\overline{\nu}$	%R	%T		$\overline{\nu}$	%R	%T
A_g	56.1	100	0	A_u	0	0	100
	66.5	100	0		32.3	0	100
	109.9	100	0		102.4	0	100
B_g	51.8	100	0	B_u	0	0	100
	102.0	100	0		0	0	100
	111.4	100	0		60.1	0	100
4T/LT	$\overline{\nu}$	%R	%T		$\overline{\nu}$	%R	%T
A_g	6.0	0	100	B_g	20.6	87	13
	37.9	35	65		28.1	20	80
	42.8	27	73		35.5	4	96
	72.8	42	58		85.5	89	11
	97.2	96	4		96.3	4	96
	112.4	98	2		111.3	96	4

and B_g phonons are present, possibly with different relative intensities, in the spectra of polycrystalline samples.

We start the analysis from the HT polymorph, which has two molecules per unit cell and therefore simpler spectra. The polarized Raman spectra of the *ab* face are shown in Fig. 5.4, the observed frequencies being reported in the first and second columns of Table 5.4. The (*bb*) polarization is not reported in the Figure, as it does not give information different from the (*aa*) one. The (*aa*) polarized spectrum allows one to easily identify 6 bands of A_g symmetry. This number is higher than expected from the RMA selection rules (Table 5.2), as some intra-molecular modes fall in the same low-frequency region of the lattice modes. It is therefore necessary to drop the RMA, and allow for the mixing of molecular and lattice modes. This is confirmed by the QHLD calculations made by relaxing the RMA, and reported in the third column of Table 5.4. In the fourth column of the Table we report the degree of mixing between lattice and molecular modes, expressed as the percentage of molecular libration (%R). The complement to 100 represents the intra-molecular character. The calculations predict 12 phonons (6 A_g and 6 B_g) with frequency below 150 cm^{-1} and at least partial inter-molecular character. All the 6 A_g phonons are indeed detected in the (*aa*) polarized

Table 5.4: Assignment of low-frequency *gerade* phonons of 4T/HT.

300 K				10 K		
Exp.[a]		Calc.[b]		Exp.[c]	Calc.[b]	
$\overline{\nu}, \parallel$	$\overline{\nu}, \perp$	$\overline{\nu}$	%R	$\overline{\nu}$	$\overline{\nu}$	Sym.
40		39.6	90	44	42.6	A_g
	40	42.1	90	46 sh	49.1	B_g
48		53.7	59	54	57.6	A_g
79		72.0	67	83 sh	78.9	A_g
	79	77.8	56	87	86.0	B_g
	100	102.8	76	112	111.3	B_g
		108.3	28		117.2	B_g
89		109.2	21	102	116.0	A_g
		118.5	27		128.0	B_g
99		123.6	40	114	133.0	A_g
121		124.5	21	128	140.2	A_g
		141.4	20		153.2	B_g

[a]Frequencies in cm^{-1}. $\parallel$ indicates the frequencies of the bands detected in the (aa) and/or (bb) polarized spectra; $\perp$ indicates the frequencies of the bands detected in the (ba) polarized spectra. Frequencies in parenthesis refer to overlapped modes. [b]Frequencies in cm^{-1}. [c]Frequencies in cm^{-1}, unpolarized spectra. sh: shoulder.

spectra, whereas only 3 B_g phonons are revealed in the (ba) spectra. Moreover, the fact that the 40 and 79 cm^{-1} bands are detected at the same frequency in the (aa) and (ba) polarized spectra (Fig. 5.4) casts some doubt on their assignment to both A_g and B_g phonons, as one might ascribe their occurrence as arising from residual polarization.

Further assistance in the identification of the modes of the 4T/HT phase comes from the comparison of the spectra of polycrystalline samples collected at 300 and 10 K, shown in the top panel of Fig. 5.5. The frequencies observed at 10 K are compared to the calculated ones at the same temperature in the 5th and 6th column of Table 5.4. By lowering the temperature at 10 K, the 300 K bands at 40 and 79 cm^{-1} develop a shoulder on the higher and lower frequency side, respectively. We then confirm the assignment proposed on the basis of the room temperature polarized spectra, with accidental quasi-degeneracy of the A_g and B_g 40 and 79 cm^{-1} phonons.

The group of broad bands between 70 and 110 cm^{-1} at 300 K narrows and shifts considerably by lowering the temperature, allowing the detection of one additional band at 114 cm^{-1}, masked in the room temperature spectra. This group of bands clearly corresponds to strongly anharmonic phonons, and their temperature evolution is properly

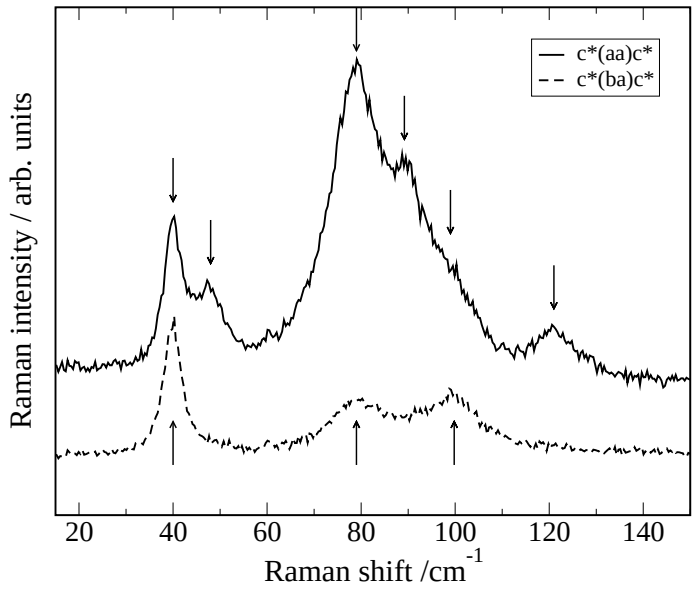

Figure 5.4: Polarized Raman spectra in the lattice phonon region of the 4T/HT polymorph ($P2_1/a$, ab plane). Downwards pointing arrows indicate A_g modes in the (aa) spectrum, upwards pointing arrows indicate B_g modes in the (ba) spectrum.

reproduced by the calculations (Table 5.4). In summary, we are able to obtain very good interpretation of the 4T/HT Raman spectra, assigning 9 out of the 12 phonons below 150 cm^{-1}. Only 3 B_g phonons of prevailing intra-molecular character are possibly too weak to be detected.

We now turn attention to the more complex 4T/LT phase, with 4 molecules per unit cell. The Raman spectra of polycrystalline samples at 300 and 10 K are reported in the bottom panel of Fig. 5.5, whereas the polarized room temperature spectra are reported in Fig. 5.6. The corresponding experimental frequencies are given in Table 5.5. In the Table we also report the calculated QHLD frequencies, together with an approximate description of the phonons at 300 K. As for 4T/HT, we have relaxed the RMA, so the librational and translational motions of the molecule mix with the intra-molecular vibrations. The percentages of librational (%R) and translational (%T) character are given in the 4th and 5th column of Table 5.5, respectively, the complement to 100 representing the intra-molecular contribution. The calculations indicate that by relaxing the RMA, 26 Raman bands (13 A_g + 13 B_g) are expected below 150 cm^{-1}.

Fig. 5.6 shows that, at variance with the HT phase, the (bb) polarization is partially different from the (aa) one, with a pair of additional bands at 37 and 41 cm^{-1}. Another difference with respect to the HT phase is the appearance of a weak A_g band at 19 cm^{-1}, barely appreciable in the (bb) spectrum, but clearly visible in the spectra of polycrystalline samples (Fig. 5.5). We associate this band to the lowest frequency A_g

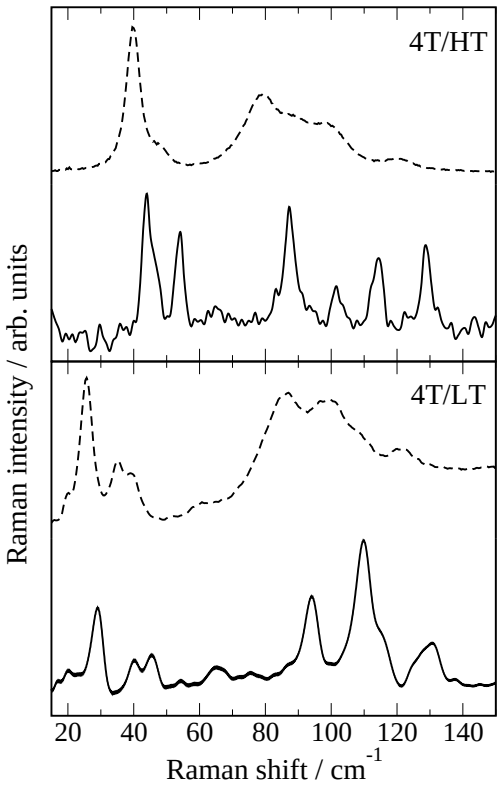

Figure 5.5: Unpolarized Raman spectra of 4T/HT and 4T/LT at 300 K (dashed lines) and 10 K (continuous lines).

mode, corresponding to the acoustic B_u phonon of the HT phase, as discussed in the previous Section. On the other hand, the Raman spectra of the LT phase, like the HT one, exhibit the intriguing frequency coincidence in the (aa) and (ba) polarizations of a low frequency, narrow, band. This band remains single also at 10 K, but, by analogy with the HT phase, we assign it to accidentally degenerate A_g and B_g phonons. In the 300 K spectra of 4T/HT the frequency coincidence occurs at 40 cm^{-1}, whereas in 4T/LT ones it is shifted to 27 cm^{-1}. Actually, this band neatly distinguishes the two phases.

Another feature the 4T/LT spectra share with the 4T/HT ones is the presence of a group of unresolved, broad bands around 100 cm^{-1}. As shown by QHLD calculations in Table 5.5, a high number of phonons are expected in this spectral region, and in the case of 4T/LT the bands are not resolved even at 10 K. The approximate description reported in the Table shows that these modes have predominant intra-molecular character, and it is not surprising they cluster in relatively narrow range. Although several modes are left unassigned, the overall interpretation of the 4T/LT Raman spectrum reported in Table 5.5 is satisfactory, considering the high number of phonons expected in the investigated spectral region, and the high degree of mixing between inter- and intra-molecular modes.

Table 5.5: Assignment of the *gerade* low-frequency phonons of 4T/LT.

300 K					10 K		
Exp.[a]		Calc.[b]			Exp.[c]	Calc.[b]	
$\overline{\nu}, \parallel$	$\overline{\nu}, \perp$	$\overline{\nu}$	%R	%T	$\overline{\nu}$	$\overline{\nu}$	Sym.
19		3.0	1	98	20	8.2	A_g
		14.4	89	8		17.8	B_g
		23.0	9	86		26.1	B_g
27		30.5	61	26	29	33.9	A_g
	27	33.1	1	96	(29)	39.7	B_g
37		35.8	1	64	40	39.6	A_g
41		40.9	23	75	45	46.6	A_g
		52.9	19	21		57.8	B_g
		54.2	39	4		59.7	B_g
		54.9	2	2	54	59.5	A_g
61		61.0	20	3	65	66.9	A_g
		65.3	7	9		71.0	B_g
		75.1	7	0		81.9	B_g
(81)		82.4	6	4	86	88.8	A_g
87		88.7	22	7	93	98.0	A_g
		93.0	2	4		99.2	B_g
100		96.6	41	8		104.3	A_g
	102	98.4	24	4	109	107.2	B_g
		101.0	24	45		112.3	B_g
(107)		106.6	56	0	116	118.2	A_g
	111	107.7	33	4	(116)	118.7	B_g
122		110.4	30	1		123.9	A_g
	119	112.9	15	7	128 sh	126.7	B_g
		118.0	15	6	126 sh	129.1	A_g
		123.4	27	6		136.6	B_g
124		128.1	16	3	131	141.1	A_g

[a]Frequencies in cm^{-1}. $\parallel$ indicates the frequencies of the bands detected in the (aa) and/or (bb) polarized spectra; $\perp$ indicates the frequencies of the bands detected in the (ba) polarized spectra. Frequencies in parenthesis refer to overlapping modes. [b]Frequencies in cm^{-1}. [c]Frequencies in cm^{-1}, unpolarized spectra. sh: shoulder.

5.5 Phase purity of 4T crystals

The QHLD method allows one to investigate the relationship between different x-ray crystal structure determinations [19], and the relative stability of the polymorphs [60].

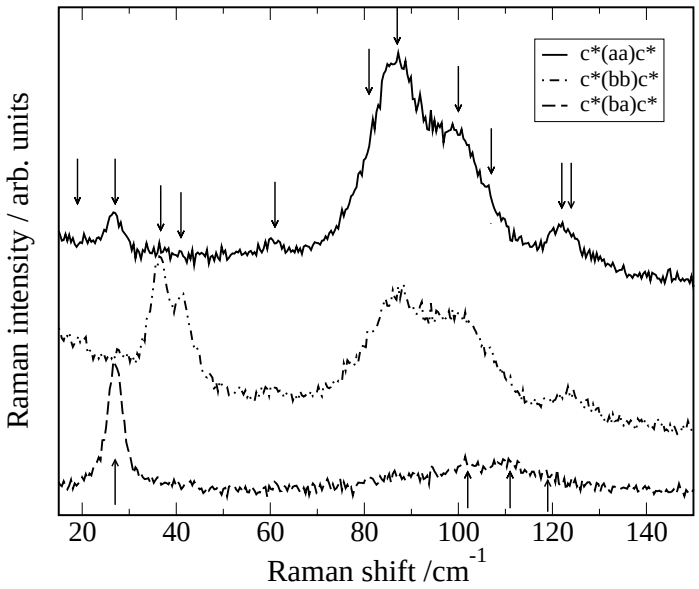

Figure 5.6: Polarized Raman spectra in the lattice phonon region of the 4T/LT polymorph ($P2_1/c$, ab plane). Downwards pointing arrows indicate A_g modes in the (aa) and (bb) spectra, upwards pointing arrows indicate B_g modes in the (ba) spectrum.

As explained in Section 4.2, in the QHLD approach one determines the crystal structures which correspond to the minimum Gibbs free energy at a given temperature.

In Table 5.6 we compare the minimum $G(p,T)$ theoretical structures computed at 300 K to the experimental structures. 4T/LT data are given in the $P2_1/c$ standard setting, while the alternative setting $P2_1/a$ has been used for 4T/HT. The structural parameters of both polymorphs are well reproduced by the calculations. The $G_{\min}$ values suggest that the HT structure is the most stable. We have indeed found that the calculation predicts the HT phase as the slightly more stable at all the temperatures. However, the LT phase is the polymorphs that grows preferentially, both from vapor phase and from solution. This suggests on the contrary that LT polymorph is the most stable phase at ambient conditions. The HT phase becomes favored only above 191 °C, a temperature quite close to the melting temperature (214 °C), and can also be obtained by heating up the LT polymorph [61, 58]. In any case, QHLD calculations indicate that the two 4T polymorphs are quite close in energy (ΔG $\approx$ 0.3 kcal/mole at 300 K, comparable to k_BT), as it happens for other organic semiconductors [53, 63, 64]. This fact raises the issue of the phase purity of the crystallites[65].

Low-frequency micro-Raman spectroscopy has been already used to show that different polymorphs can be mixed within the same crystallite [66, 65]. As shown in Fig. 5.5, the 4T/HT and 4T/LT phases can be easily discriminated by low-frequency Raman spectra. For instance, the bands at 40 cm^{-1} and at 27 cm^{-1} in 4T/HT and in 4T/LT,

Table 5.6: Lattice parameters of 4T. The experimental structures at room temperature [50] are compared to the minimum G structures calculated at 300 K.

		a (Å)	b (Å)	c (Å)	β (°)	ρ (g/cm^3)	$G_{\min}$ (kcal/mol)
HT ($P2_1/c$)	Expt.	8.935	5.751	14.340	97.22	1.511	
	Calc.[a]	8.138	5.789	14.769	96.57	1.588	−42.65
	Calc.[b]	7.618	6.022	15.622	90.35	1.532	−41.22
LT ($P2_1/a$)	Expt.	6.085	7.858	30.483	91.81	1.511	
	Calc.[a]	6.080	7.643	30.582	91.32	1.545	−42.03
	Calc.[b]	6.209	7.651	30.703	91.15	1.505	−40.94

[a]experimental x-ray molecular geometry; [b]*ab-initio* C_i molecular geometry.

respectively, are both very intense, and, with suitable corrections, representative of either polymorph in frequency ranges where the spectra of the two phases do not overlap significantly. By means of confocal Raman mapping (CRM) [66], an area of a sample is scanned with spatial resolution of 1 μm recording a Raman spectrum at each point and these bands can be used to state whether the two polymorphs are mixed at a microscopic scale.

We have then used the micro-Raman technique described in Section 4.2 to assess the phase purity of 4T crystals obtained by different crystal growth techniques. For example, samples obtained by sublimation give an essentially pure LT phase as long as the cold finger on which crystallization occurs is water-cooled and the source is kept at a temperature below 200 °C. When the temperature is raised above 200 °C, and crystals are left to grow with no external cooling, polycrystalline samples composed of a mixture of the two phases appear. Fig. 5.7 reports an example of CRM for a 4T polycrystalline sample (Fig. 5.7a) sublimed at $T = 200$ °C, $p = 10^{-2}$ Torr. The Raman maps of Fig. 5.7b, 5.7c are subsequently obtained by reporting the absolute intensities of the main peaks, diagnostic of each phase, in the same false colour palette. The comparison of the Raman maps with the optical image (Fig. 5.7a) shows how the LT phase is ingrained in the HT phase at a micrometric scale. The blue and red extremes of color visually identify the extent of either polymorph in the crystal grain. On the contrary, we have verified that the large 4T/LT single crystals grown by the floating drop technique [59] do not present phase impurity. Also the HT phase prepared by heating up the LT polymorph, that have a crystal quality degraded by the heating process, does not present inclusions of the LT phase, the conversion from 4T/LT to 4T/HT being essentially complete.

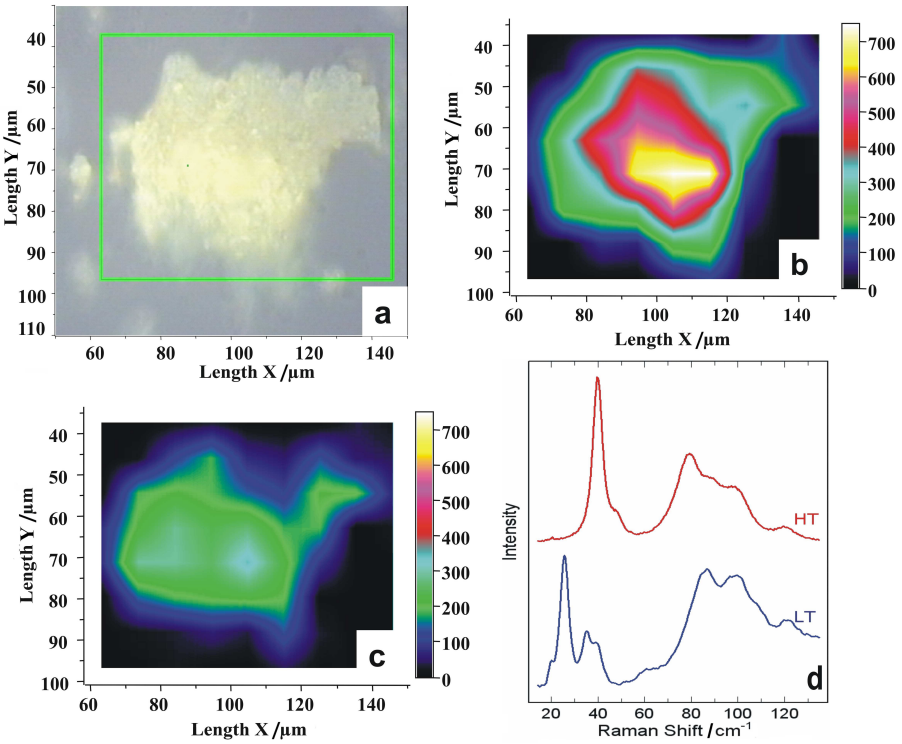

Figure 5.7: Raman mapping of a 4T polycrystalline sample obtained by sublimation (see text). a) Optical image of the sample and contour of the scanned area (green box); b), c) mapping of the intensities of the 40 cm^{-1} and 27 cm^{-1} bands, for 4T/HT and 4T/LT polymorph, respectively; d) reference spectra for the pure phases of 4T.

Chapter 6

Lattice phonons Raman spectroscopy of rubrene

6.1 Crystal structure of rubrene

The orthorhombic structure belongs to the standard space group $Cmca$ (D_{2h}^{18}), with $Z = 4$ and room temperature unit cell parameters $a = 26.901$ Å, $b = 7.187$ Å and $c = 14.430$ Å [67]. The conventional cell is non primitive (C face centered), with two molecules exchanged by a roto-translation $C_{2z} + (0, \frac{1}{2}, \frac{1}{2})$ and two more molecules obtained by a translation $\mathbf{t} = (\frac{1}{2}, \frac{1}{2}, 0)$

All molecules have C_{2h} symmetry and lie on sites with symmetry $2/m$. The molecular C_{2x} axis lies along the two central C atoms of the tetracene backbone and is parallel to the a crystal axis. The σ_{yz} mirror plane bisects the C_{2x} axis through the inversion centre. The C_{2x} axis corresponds to the short-in-plane inertia axis (*i.e.*, the one with the smallest moment) and also to the M axis. The inertia axis with the largest moment is located on σ_{yz} almost normal to the plane of the tetracene backbone, while the one with the middle moment is almost coincident with the long axis of the backbone, so that these axes are also almost coincident with the N and L axes, respectively.

6.2 Spectral prediction and selection rules

Within the RMA, the number and the symmetry of the Raman active lattice modes ($\mathbf{k} = 0$) in the $Cmca$ orthorhombic structure can be determined by considering the appropriate primitive cell with $Z = 2$. Out of the twelve lattice modes that can so be deduced, six ones are expected to be Raman active, with symmetries $A_g + 2B_{1g} + 2B_{2g} + B_{3g}$. In the absence of inter-molecular interactions, the Raman active intra-molecular vibrations of each rubrene molecule would classify as a_g or b_g species of the C_{2h} molecular symmetry group, as illustrated in Table 6.1. Since the site symmetry is a subgroup of

Table 6.1: Correlation between site and factor groups.[a]

C_{2h} site group	D_{2h}^{18} factor group	
a_g $[R_z]$	A_g	(aa, bb, cc)
	B_{3g}	(bc)
b_g $[R_x, R_y]$	B_{1g}	(ab)
	B_{2g}	(ac)

[a]We report the symmetry species of Raman active modes and the matching components of the polarizability tensor (in parentheses).

the complete $Cmca$ (D_{2h}^{18}) space group, modes of a_g and b_g species never get mixed by the crystal field. However, modes belonging to the same symmetry species on different molecules of the primitive cell do interact, leading to a splitting of the Raman active modes according to the scheme: $a_g \rightarrow A_g + B_{3g}$, $b_g \rightarrow B_{1g} + B_{2g}$.

6.3 QHLD calculations

To compute eigenvectors and vibrational frequencies of rubrene we have followed the procedure reported in Sec. 4.2. We first computed *ab initio* molecular geometry and atomic charge distribution of the isolated rubrene molecule, together with harmonic vibrational frequencies and eigenvectors of the normal modes. This was done with the Gaussian03 program [55], using the B3LYP exchange correlation functional combined with the 6-31G(d) basis set. As a starting geometry, we chose the X-ray coordinates as given in Ref.[70], adding the constraint of C_{2h} molecular symmetry. Once the energy was minimized with the required symmetry, harmonic frequencies for the molecular vibrations could be calculated and then scaled by the factor of 0.9613 recommended [57] for the combination of B3LYP and 6-31G(d). With this procedure, the ungerade vibrational mode describing the butterfly motion of the two pairs of phenyl substituents in C_{2h} rubrene turned out to have an imaginary frequency. This means that the C_{2h} conformation does not correspond to a minimum energy geometry for the isolated molecule, but rather to a saddle point. This is in agreement with previous calculations [68] reporting that rubrene exhibits in the solid state a geometry different from that of the gas phase, which is calculated to have D_2 symmetry and corresponds to the global minimum of the isolated molecule potential. To overcome the problem of the imaginary frequency in rubrene crystal, we adopted the usual strategy, which consists in optimizing the energy of a molecule slightly deformed along the mode(s) with imaginary frequency. In the case of C_{2h} rubrene the removal of the inversion centre gives symmetry C_2. This procedure assures a set of real frequencies (and corresponding eigenvectors) computed

at a geometry as close as possible to that observed in the crystal. The optimized C_{2h} molecular geometry was employed in the input of the lattice dynamics calculations as described in Section 4.2. As usual, the crystal was initially described in terms of rigid molecules (RMA), in order to have a good starting reference point for the subsequent calculation without the RMA. The computation of rubrene lattice phonons with the RMA method and by introducing the phonon-phonon coupling is reported in Table 6.2.

6.4 Lattice-phonons Raman spectra and spectral assignment

We have measured the Raman spectra of rubrene crystal in polarized light, with special emphasis on the lattice phonon region, by using a variety of vapor grown specimens. Most of them are platelets of elongated irregular hexagonal shape, but also a few needles were obtained. We did not identify the crystal planes of our samples by X-ray measurements, but both platelets and needles were oriented in each experiment with the aid of a polarizing microscope, to ensure that the principal axes of the dielectric tensor were coincident with the extinction directions. Following the literature [69, 70], we assumed the flat face of the platelet to be *bc*, with *b* the elongated axis. For the needles, we assumed [67, 71] that the direction of fastest growth coincides with that of strongest inter-molecular interactions, i.e. *b*.

Figure 6.1 shows polarized Raman spectra of rubrene platelets in the region of the lattice phonons and of the lowest energy molecular vibrations. Figure 6.2 shows polarized Raman spectra of rubrene needles in the same energy range.

From the symmetry of the polarizability tensor we can state that for the platelets the A_g symmetry modes are allowed in the *bb* configuration, whereas the B_g can be detected in the *bc* configuration. The spectra of the needles obtained from the *bc* face should be indistinguishable from those of platelets. When we analyze the *ab* face, accessible by rotating the crystal of 90° around the *b*-axis, A_g modes are present in the *bb* or *aa* configuration, whereas B_{1g} are detectable in the *ab* configuration.

Our analysis starts by comparing the spectra of needles and platelets (Figures 6.1 and 6.2). Typically, by rotating the needles around the growth axis *b*, we have obtained two different patterns in the spectra, as can be seen in Figure 6.2. One of these patterns coincides with what observed for platelets (Figure 6.1), showing that in this case we measure the Raman scattering from the *bc* crystal surface. The other pattern differs in the number and in the relative intensities of bands. Note especially how the relative intensity of total symmetric bands can change dramatically in the two patterns, clearly depending on which diagonal element of the Raman tensor is probed in each experiment. The straightforward explanation for this is that we are now probing the needle *ab* surface. This conclusion is supported by the analysis of selected polarized bands in the higher

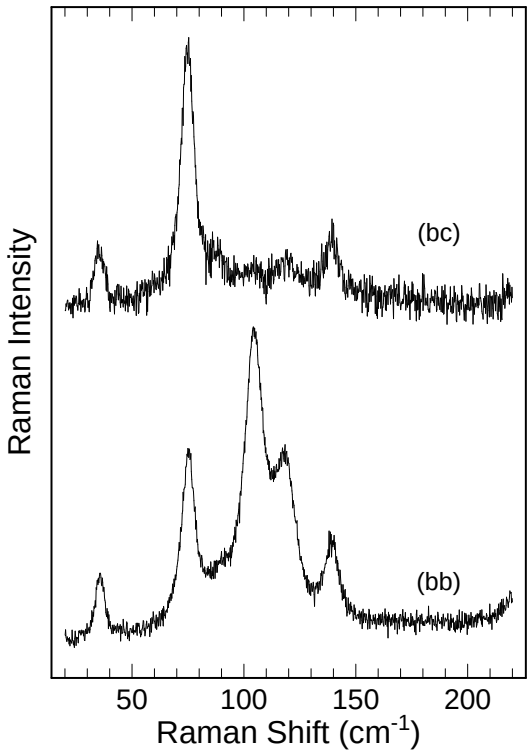

Figure 6.1: Polarized spectra of rubrene crystal platelets in the low energy region. Platelets have been oriented with a polarizing microscope, with the flat *bc* surface of the *Cmca* orthorhombic structure normal to the incoming light. In parentheses the components of the polarizability tensor probed in the experiment.

energy range, bearing in mind that the B_{1g} components of b_g molecular vibrations should be only visible when *ab* surfaces are accessed. This is true, for instance, for the weak band at 206.6 cm observed in the spectrum labeled as (*ab*) in Figure 6.2. This band originates from the B_{1g} component of an intra-molecular mode calculated at 205.0 cm^{-1}in the crystal (see Table 6.2), and never appears in the spectra labeled as (*bc*) of either platelets or needles. Even more clear evidence is given by the vibrational analysis between 1400 and 1600 cm^{-1}: in Figure 6.3 we compare the polarized spectra of a platelet and of a needle which is *ab* oriented. The two strong bands at 1520.8 and 1616 cm^{-1}labeled as (*ab*) in the needle spectrum are assigned to the B_{1g} components of molecular modes calculated *ab-initio* at 1490 and 1593 cm^{-1}, respectively. They are almost absent, as expected, in the platelet spectrum. In the same energy range the most intense total symmetric band both in the *bb* spectra of needles and *cc* spectra of platelets lies at 1432.1 cm^{-1}, and corresponds to the a_g molecular mode calculated *ab-initio* at 1422.5 cm^{-1}.

B_{2g} modes, although Raman active, are not straightforwardly observed in single

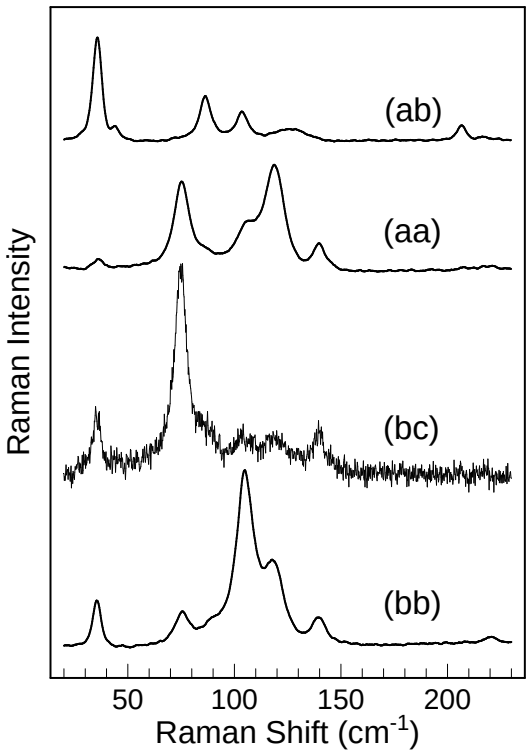

Figure 6.2: Polarized spectra of rubrene crystal needles in the low energy region. Needles have been oriented along the b axis; top: the backscattering is collected from the ab surface of the $Cmca$ orthorhombic structure; bottom: the backscattering is collected from the bc surface. In parentheses the components of the polarizability tensor probed in the experiment.

crystals. The analysis of the powder spectrum, as reported Figure 6.4 reveals two more bands at 45.8 and 89.4 cm^{-1}which are observed here as strong but have very low intensity in the spectra of either platelets or needles. These bands are tentatively assigned to B_{2g} phonons.

The symmetry assignments given in Table 6.2 are therefore made on the basis of the comparison among four different sources of spectra: needles both ab and bc oriented; platelets; powder (to which, of course, polarization is not applicable) and the results of the calculations, also reported in the Table. We need to comment about the number and the origin of some accidental degeneracies given in the Table, in particular the overlap of bands assigned to modes with A_g, B_{1g} and B_{3g} symmetries around 35 cm^{-1}, and the overlap of bands assigned to modes with A_g and B_{3g} symmetry around 75 cm^{-1}. The assignment of the lowest energy B_{1g} mode is supported on one hand by the experimental evidence, as this bands dominates the spectrum labeled as (ab) of Figure 6.2, and on the other hand by the calculations, which predict a lattice phonon mode in this range

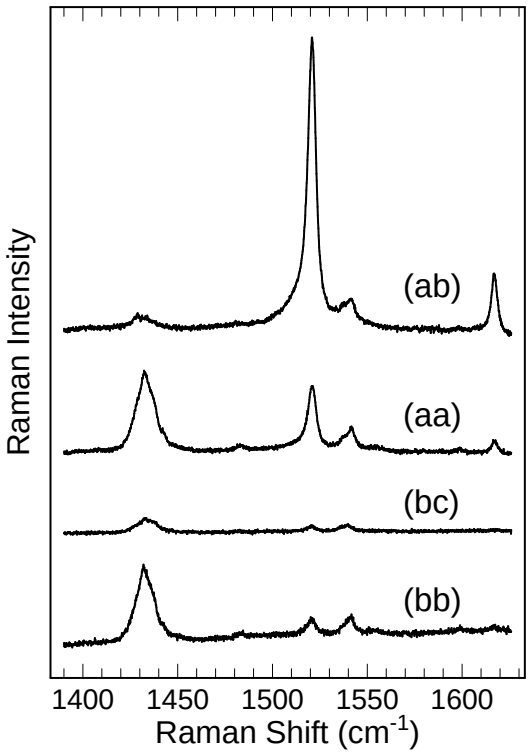

Figure 6.3: Polarized spectra of rubrene crystal needles and platelets between 1400 and 1600 cm^{-1}. Needles have been oriented along the b axis; top: the backscattering is collected from the ab surface of the $Cmca$ orthorombic structure; bottom: the backscattering of the platelet is collected from the bc surface. In parentheses the components of the polarizability tensor probed in the experiment.

in both in RMA and FMA methods. So, we are fully confident about the correctness of this assignment. Similar considerations apply to the two B_{3g} bands, which are found to appear as quite strong in all the spectra labeled as (bc), and whose assignment is also supported by the calculations. Admittedly, the assignment of the 35 cm^{-1} A_g mode is more dubious, as this band is very weak in most of the recorded spectra. The precision of the positioning of the samples on the microscope stage allows us to exclude the effect of residual polarization resulting from poor alignment along the principal axes of the platelet. However, we cannot rule out, as outlined before, the presence of scattering from faces not matching the bc surface. Finally, one should not forget that many bands are expected over a very narrow energy interval, so that either accidental overlaps are very likely to occur, or very weak bands can escape detection.

In summary, by combining polarized spectra with computational methods, we have been able to obtain an almost complete assignment and characterization of the low-energy phonons. The task has been a challenging one, since many molecular modes

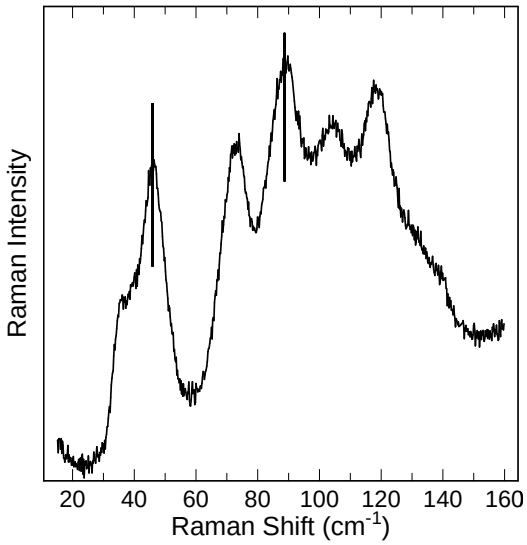

Figure 6.4: Spectrum of crystalline rubrene powder. Vertical bars mark the bands assigned to B_{2g} modes.

of the isolated rubrene molecule fall in the same spectral region of the inter-molecular phonons. The QHLD calculations indeed show that 21 phonons are expected below 200 cm^{-1} (Table 6.2). As a consequence, there is strong mixing between intra- and inter-molecular modes.

Table 6.2: Raman frequencies (cm^{-1}) for crystalline rubrene.

Experimental		FMA calculations		RMA calculations	
$\overline{\nu}$	Sym.	$\overline{\nu}$	$\%^b$	$\overline{\nu}^c$	Sym.^{d}
35.5	A_g	48.5	41.4	20.3	a_g
75.3	A_g	55.3	36.3	64.2	a_g
104.8	A_g	103.7	5.9	70.4	A_g
118.6	A_g	108.1	14.6	81.0	a_g
139.6	A_g	156.7	1.5	128.8	a_g
220.2	A_g	217.9	0.1	205.7	a_g
35.5	B_{1g}	33.9	96.6	39.1	B_{1g}
43.9	B_{1g}	47.2	93.4	55.3	B_{1g}
86.3	B_{1g}	82.9	2.8	70.6	b_g
103.7	B_{1g}	105.4	3.9	80.1	b_g
123.0	B_{1g}	119.7	2.3	94.1	b_g
-	B_{1g}	173.3	0.7	149.7	b_g
206.6	B_{1g}	205.0	0.2	193.0	b_g
45.8^e	B_{2g}	29.3	96.0	38.4	B_{2g}
-	B_{2g}	60.8	85.4	68.3	B_{2g}
89.4^c	B_{2g}	93.2	10.1	70.6	b_g
35.5	B_{3g}	35.1	30.8	20.3	a_g
75.3	B_{3g}	81.5	24.6	64.2	a_g
87.4	B_{3g}	91.0	41.0	76.6	B_{3g}
104.0	B_{3g}	101.1	3.0	81.0	a_g
139.2	B_{3g}	151.2	0.5	128.8	a_g

[a]We report the experimental frequencies of lattice and low energy intra-molecular modes, with symmetry assignments, and the results of FMA and RMA calculations at 300 K. [b]Percentage of lattice phonons in the squared eigenvectors. [c]RMA frequencies or *ab initio* results for the isolated molecule. [d] Symmetry species of the D_{2h}^{18} space group or the C_{2h} site group for RMA or *ab initio* results (upper or lower case, respectively). [e] Values from the spectra of powder samples.

Conclusions

The first part of the thesis has been devoted to mixed stack CT crystals that undergo the neutral-ionic phase transition when an external parameter, like temperature or pressure, is modified. The ionic phase can have weak ferroelectric properties, whose improvement may eventually lead to the development of new organic devices.

We have investigated the temperature-induced neutral-ionic phase transition in the CT mixed-stack crystals dimethyltetrathiafulvalene-chloranil. The strong variations in the vibrational spectra induced by the electronic and structural changes makes infrared and Raman spectroscopy a quite convenient tool to characterize this kind of phase transition. In particular, we have shown that the molecular charge continuously increases by lowering the temperature and the stack dimerizes below 65 K. Intermolecular dipolar moments, formed in this low temperature phase have an *antiferroelectric* arrangement. In addition, we have evidenced the role of the phonons in driving the structural transition. We have indeed demonstrated how the Peierls mechanism can be invoked to rationalize the dimerization transition. This mechanism appears to be the driving force of the transition, and the variation in the molecular charge is probably a consequence of the structural rearrangement.

Another well-studied mixed stack CT crystal, tetrathiafulvalene-chloranil, has been considered due to its ferroelectric state below 81 K. We have studied the effect of a static electric field on the molecular charge and on the dimerization, by observing the variation of the vibrational infrared spectra. The transformations induced by the electric field on this ferroelectric are at the moment not easy to rationalize. The most evident effects are the ability of the field to change the molecular charge, in particular to lower it. This correspond to shift the system towards the neutral side, with the possibility to switch from the ionic to the neutral phase. The structural variations are in the same direction, namely, we pass from the dimerized to the regular phase. The most evident signature of the ferroelectricity is the memory effects displayed by repeated application of the electric field. For instance, the critical value of the electric field necessary to switch from the ionic to the neutral phase changes depending on the number of times the switching has been induced. In addition, we observe a large hysteresis in the phase switching. These phenomena make this ferroelectric system very interesting and worth further studies.

In the second part of the thesis we have studied single component organic semiconductors. The increasing interest in organic electronics requires accurate investigation of the physical properties affecting the performance of the active material. Polymorphism is one of the factor that degrades the technological requirements, like carrier mobility, of many potential organic devices. Polymorphism quite often yields phase mixing. The careful phase control of polymorphic materials is of paramount importance whenever phase purity is a strict requirement in sample preparation. Phase homogeneity cannot be taken for granted, even for well formed single crystals. Different polymorphs can coexist down to the μm scale and physical inhomogeneities occur at surfaces and in the bulk. Different crystalline polymorphs can be conveniently probed by their Raman spectra in the region of the lattice phonons (usually below 150 cm^{-1}), whose frequencies depend the inter-molecular interactions and turn out to be very sensitive to differences in molecular packing. The method we have illustrated, lattice phonon confocal Raman mapping, is a powerful technique to probe the crystal structure of organic materials, being fast, reliable and capable to monitor in situ physical modifications and phase inhomogeneities in crystal domains at the micrometer scale. Comparison of optical images and Raman maps conclusively shows that no relationship exists between morphology and crystal phase. Structural information is better obtained from Raman images. It is then crucial to perform a spectroscopic test in order to verify the phase purity in all crystals treated, especially for those cases in which crystal morphology cannot assist phase recognition.

With this technique we have investigated the polymorphism in the organic semiconductors α-quaterthiophene and rubrene. The application of the Raman mapping method requires an accurate knowledge of the lattice phonons of the particular crystal structure and a complete assignment of the symmetry of the phonons. This has been obtained by combining polarized spectra with computational methods. In this way we have the possibility to identify with certainty some particular phonons characteristic of a specific crystal structure. Then by means of lattice phonons we have discerned the two polymorphic phases of α-quaterthiophene, and showed that they can coexist in certain conditions of the crystal growth. On the contrary, rubrene does not show the presence of different polymorphs even if two different crystal habits can be obtained during the crystal growth. We have also obtained a reliable description of the lattice phonon dynamics in these two organic semiconductors, which is a fundamental prerequisite for the understanding of the still widely debated mobility mechanism.

Bibliography

[1] J. B. Torrance, J. E. Vasquez, J. J. Mayerle, V. Y. Lee, Phys. Rev. Lett. **46**, 253 (1981); J. B. Torrance, A. Girlando, J. J. Mayerle, J. I. Crowley, V. Y. Lee, P. Batail, S. J. LaPlaca, Phys. Rev, Lett. **47**, 1747 (1981).

[2] Z. G. Soos, S. A. Bewick, A. Painelli, A. Girlando, Synth. Metals **155**, 357 (2005)

[3] S. Horiuchi, T. Hasegawa, Y. Tokura, Chem. Phys. **75**, 051016 (2006).

[4] A. Painelli, A. Girlando, J. Chem. Phys. **84**, 5655 (1986).

[5] C. Pecile, A. Painelli, A. Girlando Mol. Cryst. Liq. Cryst. **171**, 69 (1989).

[6] A. Girlando, I. Zanon, R. Bozio, C. Pecile J. Chem. Phys. **68**, 22 (1978).

[7] P. Ranzieri, M. Masino, A. Girlando, J. Phys. Chem. B **111**, 12844 (2007).

[8] A. Girlando, A. Painelli, S. A. Bewick, Z. G. Soos, Synth. Metals **141**, 129 (2004) and references therein.

[9] S. Horiuchi, R. Kumai, Y. Okimoto, Y. Tokura, Chem. Phys. **325**, 78 (2006); S. Horiuchi, T. Hasegawa, Y. Tokura, J. Phys. Soc. Japan **75**, 051016 (2006)

[10] S. Horiuchi, Y. Okimoto, R. Kumai, Y. Tokura, J. Am. Chem. Soc. **123**, 665 (2001).

[11] S. Horiuchi, Y. Okimoto, R. Kumai, Y. Tokura, Science **299**, 229 (2003).

[12] Y. Okimoto, R. Kumai, S. Horiuchi, H. Okamoto, Y. Tokura, J. Phys. Soc. Japan **74**, 2165 (2005).

[13] S. Aoki, T. Nakayama, A. Miura, Phys. Rev. B **48**, 626 (1993).

[14] E. Collet, M. Buron-Le Cointe, M. H. Lemée-Cailleau, H. Cailleau, L. Toupet, M. Meven, S. Mattauch, G. Heger, N. Karl, Phys. Rev. B **63**, 054105 (2001).

[15] E. Collet, M. H. Lemée-Cailleau, M. Buron-Le Cointe, H. Cailleau, S. Ravy, T. Luty, J. F. Bérar, P. Czarnecki, N. Karl, Europhys. Lett. **57**, 67 (2002).

[16] F. Iwase, K. Miyagawa, S. Fujiyama, K. Kanoda, S. Horiuchi, Y. Tokura, J. Phys. Soc. Japan **76**, 073701-1 (2007).

[17] A. Girlando, F. Marzola, C. Pecile, J. B. Torrance, J. Chem. Phys. **79**, 1075 (1983).

[18] M. Masino, A. Girlando, Z. G. Soos, Chem. Phys. Lett. **369**, 428 (2003).

[19] M. Masino, A. Girlando, A. Brillante, R. G. Della Valle, E. Venuti, N. Drichko, M. Dressel, Chem. Phys. **325**, 71 (2006).

[20] C. Katan, P. E. Blochl, P. Margl, C. Koenig, Phys. Rev. B **53**, 12112 (1996).

[21] A. Painelli, L. Del Freo, Z. G. Soos, Synth. Metals **133-134**, 619 (2003).

[22] M. D. Fontana, G. Métrat, J. L. Servoin, F. Gervais, J. Phys. C **16**, 483 (1984).

[23] Z. G. Soos, S. A. Bewick, A. Peri, A. Painelli, J. Chem. Phys **120**, 6712 (2004).

[24] W. K. Kwok, U. Welp, K. D. Carlson, G. W. Crabtree, K. G. Vandervoort, H. H. Wang, A. M. Kini, J. M. Williams, D. L. Stupka, L. K. Montgomery, J. E. Thompson, Phys. Rev. B **42**, 8686 (1990).

[25] V. Oison, P. Rabiller, C. Katan, J. Phys. Chem. A **108**, 11049 (2004).

[26] S. H. Walmsley, D. P. Craig, Excitons in molecular crystals: Theory and Applications, Benjamin, New York, 1968.

[27] M. Avignon, C. A. Balseiro, C. R. Proetto, B. Alascio, Phys. Rev. B **33**, 205 (1986).

[28] B. Horovitz, J. Solyom, Phys. Rev. B **35**, 7081 (1987).

[29] N. Nagaosa, J. Phys. Soc. Japan **55**,2754 (1986).

[30] K. Yonemitsu, Phys. Rev. B **65**, 205105 (2002).

[31] S. Koshihara, Y. Koshihara, H. Sakai, Y. Tokura, T. Luty, J. Phys. Chem. B **103**, 2592 (1999).

[32] E. Collet, Ph. D. Thesis.

[33] H.Kishida, K. Fujinuma, H. Okamoto, Synthetic Metals **120**, 909 (2001).

[34] Y. Tokura, H. Okamoto, T. Koda, T. Mitani, G. Saito, Phys. Rev. B **38**, 2215 (1988).

[35] B. K. Crone, *et. al.*, J. Appl. Phys. **89**, 5125 (2001).

[36] M. Lefenfeld, *et. al.*, Adv. Mater. **15**, 1188 (2003).

[37] H. E. A. Huitema, *et. al.*, Nature **414**, 599 (2001).

[38] R. H. Friend, R. W. Gymer, A. B. Holmes, J. H. Burroughes, R. N. Marks, C. Taliani, Nature **397**, 121 (1999).

[39] J. H. Burroughes, D. D. C. Bradley, A. R. Brown, R. N. Marks, Nature **347**, 539 (1990).

[40] C. W. Tang, S. A. Van Slyke, Appl. Phys. Lett. **51**, 913 (1987).

[41] J. R. Sheats, H. Antoniadis, M. Hueschen, W. Leonard, J. Miller, R. Moon, D. Roitman, A. Stocking, Sciene **273**, 884 (1996).

[42] A. Brillante, R. G. Della Valle, L. Farina, A. Girlando, M. Masino and E. Venuti, Chem. Phys. Letters, **357**, 32 (2002).

[43] T. Siegrist T, C. Besnard, S. Haas, M. Schiltz, P. Pattison, D. Chernyshov, B. Batlogg and C. Kloc, Adv. Mater., **19**, 2079 (2007).

[44] E. Venuti, R. G. Della Valle, L. Farina, A. Brillante, M. Masino and A. Girlando, Phys. Rev. B, **70**, 104106/1 (2004).

[45] A. Brillante, I. Bilotti, F. Biscarini, R. G. Della Valle, and E. Venuti, Chem. Phys., **328**, 125 (2006).

[46] C. C. Mattheus, G. A. de Wijs, R. A. de Groot and T. T. M. Palstra, J. Am. Chem. Soc., **125**, 6323 (2003).

[47] C. C. Mattheus, A. B. Dros, J. Baas, G. T. Oostergetel, A. Meetsma, J. L. de Boer and T. T. M. Palstra, Synth. Metals, **138**, 475 (2003).

[48] A. Brillante, I. Bilotti, C. Albonetti, J-F. Moulin, P. Stoliar, F. Biscarini and D. M. de Leeuw, Adv. Funct. Mater., **17**, 3119 (2007).

[49] R. A. Laudise, C. Kloc, P. Simpkins, T. Siegrist, J. Cryst. Growth **187**,449 (1998).

[50] T. Siegrist, C. Kloc, R. A. Laudise, H. E. Katz, R. C. Haddon, Adv. Mater. **10**, 379 (1998).

[51] L. Antolini, G. Horowitz, F. Kouki, F. Garnier, Adv. Mater. **10**, 382 (1998).

[52] G. Turrel, *Infrared and Raman Spectra of Crystals*, Academic Press, London, **1972**.

[53] E. Venuti, R. G. Della Valle, L. Farina, A. Brillante, M. Masino, A. Girlando, Phys. Rev. B **70**, 104106-1 (2004).

[54] A. Girlando, M. Masino, G. Visentini, R. G. Della Valle, A. Brillante, E. Venuti, Phys. Rev. B **62**, 14476 (2000).

[55] M. J. Frisch, G. W. Trucks, H. B. Schlegel, G. E. Scuseria, M. A. Robb, J. R. Cheeseman, J. A. Montgomery, Jr., T. Vreven, K. N. Kudin, J. C. Burant, J. M. Millam, S. S. Iyengar, J. Tomasi, V. Barone, B. Mennucci, M. Cossi, G. Scalmani, N. Rega, G. A. Petersson, H. Nakatsuji, M. Hada, M. Ehara, K. Toyota, R. Fukuda, J. Hasegawa, M. Ishida, T. Nakajima, Y. Honda, O. Kitao, H. Nakai, M. Klene, X. Li, J. E. Knox, H. P. Hratchian, J. B. Cross, V. Bakken, C. Adamo, J. Jaramillo, R. Gomperts, R. E. Stratmann, O. Yazyev, A. J. Austin, R. Cammi, C. Pomelli, J. W. Ochterski, P. Y. Ayala, K. Morokuma, G. A. Voth, P. Salvador, J. J. Dannenberg, V. G. Zakrzewski, S. Dapprich, A. D. Daniels, M. C. Strain, O. Farkas, D. K. Malick, A. D. Rabuck, K. Raghavachari, J. B. Foresman, J. V. Ortiz, Q. Cui, A. G. Baboul, S. Clifford, J. Cioslowski, B. B. Stefanov, G. Liu, A. Liashenko, P. Piskorz, I. Komaromi, R. L. Martin, D. J. Fox, T. Keith, M. A. Al-Laham, C. Y. Peng, A. Nanayakkara, M. Challacombe, P. M. W. Gill, B. Johnson, W. Chen, M. W. Wong, C. Gonzalez, J. A. Pople, *Gaussian03, revision D.02*, Gaussian, Inc., Wallingford CT, **2004**.

[56] W. D. Cornell, P. Cieplak, C. I. Bayly, I. R. Gould, K. M. Merz Jr., D. M. Ferguson, D. C. Spellmeyer, T. Fox, J. W. Caldwell, P. A. Kollman, J. Am. Chem. Soc., **117**, 5179 (1995).

[57] J. P. Merrick, D. Moran, L. Radom, J. Phys. Chem. A, **111**, 11683 (2007).

[58] M. Campione, S. Tavazzi, M. Moret, W. Porzio, J. Appl. Phys. **101**, 083512 (2007).

[59] M. Campione, R. Ruggerone, S. Tavazzi, M. Moret, J. Mater. Chem. **15**, 2437 (2005).

[60] R. G. Della Valle, E. Venuti, A. Brillante, A. Girlando, J. Chem. Phys. **118**, 807 (2003).

[61] S. Tavazzi, M. Campione, Appl. Phys. Lett. **88**, 071918 (2006).

[62] J. D. Dunitz, J. Bernstein, Acc. Chem. Res. **28**, 193 (1995).

[63] A. Brillante, R. G. Della Valle, L. Farina, A. Girlando, M. Masino, E. Venuti, Chem. Phys. Lett. **357**, 32 (2002).

[64] A. Brillante, I. Bilotti, F. Biscarini, R. G. Della Valle, E. Venuti, Chem. Phys. **328**, 125 (2006).

[65] A. Brillante, I. Bilotti, R. G. Della Valle, E. Venuti, M. Masino, and A. Brillante, Adv. Mater. **17**, 2549 (2005).

[66] A. Brillante, I. Bilotti, R. G. Della Valle, E. Venuti, A. Girlando, CrystEngComm **10**, 937 (2008).

[67] Chapman, B. D.; Checco, A.; Pindak, R.; Siegrist, T.; Kloc, Ch., Journal of Crystal Growth **290**, 479 (2006).

[68] D. Kafer, L. Ruppel, G. Witte, C. Woll, Phys. Rev. Lett. **95**, 166602 (2005).

[69] Menard, E.; Marchenko, A.; Podzorov, V.; Gershenson, M. E.; Fichou, D.; Rogers, J. A., *Adv. Mater.* **18**, 1552 (2006).

[70] Jurchescu, O. D.; Meetsma, A.; Palstra, T. T. M., *Acta Cryst. B* **62**,330 (2006).

[71] de Boer, R. W. I.; Gershenson, M. E.; Morpurgo, A. F.; Podzorov, V., *Phys. Stat. Sol.* (a) **201**, 1302 (2004).